

AD-A178 264

VISCOUS-INVISCID INTERACTION WITH HIGHER-ORDER  
VISCOUS-FLOW EQUATIONS: AP. (U) IOWA INST OF HYDRAULIC  
RESEARCH IOWA CITY S YOO ET AL. MAR 87 IHR-387

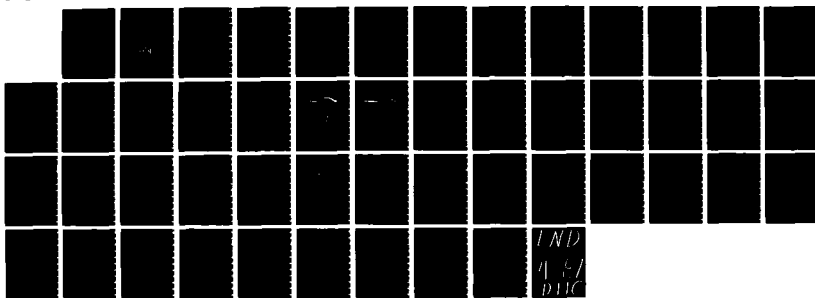
1/1

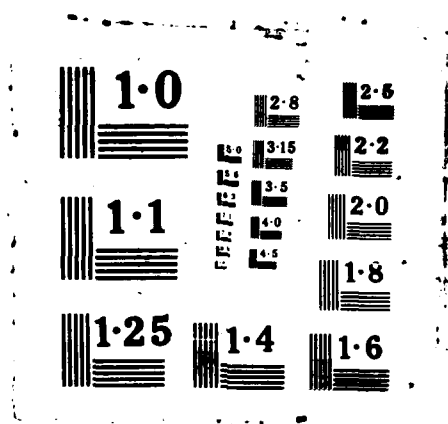
UNCLASSIFIED

NO0014-83-K-0136

F/8 20/4

ML





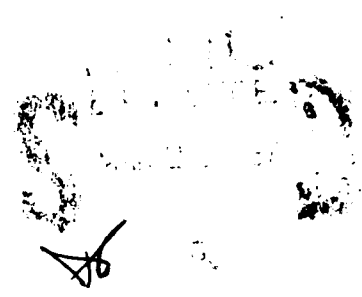
12

# VISCOUS-INVISCID INTERACTION WITH HIGHER-ORDER VISCOUS-FLOW EQUATIONS: APPLICATIONS TO THREE-DIMENSIONAL BODIES

by

S. Y. Yoo, F. Stern, and V. C. Patel

AD-A178 264



IIHR Report No. 307

Iowa Institute of Hydraulic Research  
The University of Iowa  
Iowa City, Iowa 52242

March 1987

# VISCOUS-INVISCID INTERACTION WITH HIGHER-ORDER VISCOUS-FLOW EQUATIONS: APPLICATIONS TO THREE-DIMENSIONAL BODIES

by

S. Y. Yoo, F. Stern, and V. C. Patel

IIHR Report No. 307

Iowa Institute of Hydraulic Research  
The University of Iowa  
Iowa City, Iowa 52242

March 1987

**VISCOUS-INVISCID INTERACTION WITH  
HIGHER-ORDER VISCOUS-FLOW EQUATIONS:  
APPLICATIONS TO THREE-DIMENSIONAL BODIES**

by

S.Y. Yoo, F.Stern, and V.C. Patel

Sponsored by

Office of Naval Research  
Accelerated Research Initiative (Special Focus)  
Program in Ship Hydrodynamics  
Contract No. N00014-83-K-0136



Accession For	
NTIS GRA&I	
DTIC TAB	
Unannounced	
Justification	
By	
Date	
For	
File	
Index	
Abstract	
Notes	
Microfilm	
microfiche	
Other	

At

IIHR Report No. 307

Iowa Institute of Hydraulic Research  
The University of Iowa  
Iowa City, Iowa 52242

March 1987

Approved for Public Release: Distribution Unlimited

Unclassified

SECURITY CLASSIFICATION OF THIS PAGE (When Data Entered)

REPORT DOCUMENTATION PAGE		READ INSTRUCTIONS BEFORE COMPLETING FORM
1. REPORT NUMBER IIHR Report No. 307	2. GOVT ACCESSION NO.	3. RECIPIENT'S CATALOG NUMBER
4. TITLE (and Subtitle) Viscous-Inviscid Interaction with Higher-Order Viscous-Flow Equations: Applications to Three Dimensional Bodies	5. TYPE OF REPORT & PERIOD COVERED Technical Report September 1986 - March 1987	
7. AUTHOR(s) Sungyul Yoo, Frederick Stern, and Virendra C. Patel	6. PERFORMING ORG. REPORT NUMBER IIHR Report No. 307	
9. PERFORMING ORGANIZATION NAME AND ADDRESS Iowa Institute of Hydraulic Research The University of Iowa Iowa City, Iowa 52242-1585	8. CONTRACT OR GRANT NUMBER(s) N00014-83-K-0136	
11. CONTROLLING OFFICE NAME AND ADDRESS Office of Naval Research 800 North Quincy Street Arlington, Virginia 22217	10. PROGRAM ELEMENT, PROJECT, TASK AREA & WORK UNIT NUMBERS NR 655-002	
14. MONITORING AGENCY NAME & ADDRESS (if different from Controlling Office) Office of Naval Research 536 South Clark Street Chicago, Illinois 60605	12. REPORT DATE March 1987	
	13. NUMBER OF PAGES 40	
	15. SECURITY CLASS. (of this report) Unclassified	
	15a. DECLASSIFICATION/DOWNGRADING SCHEDULE	
16. DISTRIBUTION STATEMENT (of this Report) Approval for Public Release		
17. DISTRIBUTION STATEMENT (of the abstract entered in Block 20, if different from Report)		
18. SUPPLEMENTARY NOTES		
19. KEY WORDS (Continue on reverse side if necessary and identify by block number) Thick 3-D Boundary Layer, Viscous-Inviscid Interaction, Partially-Parabolic Equations, Computational Fluid Dynamics		
20. ABSTRACT (Continue on reverse side if necessary and identify by block number) A viscous-inviscid interaction method for three-dimensional flows, in which the partially-parabolic Reynolds equations are coupled with an inviscid-flow solution procedure in an interactive and iterative manner, is applied to two simple three-dimensional bodies for which experimental data are available for comparison. The relative merits of interactive and global solution procedures are evaluated by comparing the viscous-inviscid interaction solutions with nonin- teractive large-domain solutions of only the viscous-flow equations. Both meth- ods yield satisfactory results, although the interaction solutions are found to be computationally more efficient for the cases considered.		

DD FORM 1 JAN 73 1473

EDITION OF 1 NOV 65 IS OBSOLETE  
S/N 0102-LF-014-6601

Unclassified

SECURITY CLASSIFICATION OF THIS PAGE (When Data Entered)

## ABSTRACT

A viscous-inviscid interaction method for three-dimensional flows, in which the partially-parabolic Reynolds equations are coupled with an inviscid-flow solution procedure in an interactive and iterative manner, is applied to two simple three-dimensional bodies for which experimental data are available for comparison. The relative merits of interactive and global solution procedures are evaluated by comparing the viscous-inviscid interaction solutions with noninteractive large-domain solutions of only the viscous-flow equations. Both methods yield satisfactory results, although the interaction solutions are found to be computationally more efficient for the cases considered.

## ACKNOWLEDGEMENTS

This research was sponsored by the Office of Naval Research, Accelerated Research Initiative (Special Focus) Program in Ship Hydrodynamics, under Contract N00014-83-K-0136. The Graduate College of The University of Iowa provided a large part of the computer funds.

## TABLE OF CONTENTS

	Page
Abstract.....	i
Acknowledgements.....	1
I. Introduction.....	1
II. Outline of the Computational Method.....	1
III. Extensions for Three-Dimensional Flow.....	3
IV. Applications to Three-Dimensional Bodies.....	3
A. Elliptical Cross-Section Bodies.....	3
B. Calculations.....	4
C. Results and Discussion.....	5
V. Concluding Remarks.....	9
References.....	10
Figures.....	11
Appendix I Corrections to Stern et al. (1986).....	33
Appendix II Modifications of Equations in Discretized Form for Three-Dimensional Flows.....	35

## I. INTRODUCTION

Recently, the authors (Stern et al., 1986) described a viscous-inviscid interaction method for three-dimensional flows which require equations more general than the classical boundary-layer equations. The method couples the partially-parabolic Reynolds equations with an inviscid-flow solution procedure in an interactive and iterative manner. The relative merits of interactive and global solution procedures were evaluated by comparing the interaction solutions and large-domain solutions of only the viscous-flow equations with experimental data and other computational methods for two-dimensional and axisymmetric bodies. Both methods were found to be satisfactory, and the results clearly demonstrated the feasibility of higher-order viscous-inviscid interaction procedures.

This report describes the results from applications of the aforementioned methods to two simple three-dimensional bodies. Since the computational method is described in the previous report it suffices here to provide an outline. However, during the course of the present calculations it was found that modifications of some of the finite-difference formulas were required to deal with three-dimensional bodies. These are provided here. Also, corrections to errors in the text of Stern et al. (1986), discovered after printing, are given in Appendix I.

## II. OUTLINE OF THE COMPUTATIONAL METHOD

Consider the flow past a streamlined three-dimensional body fixed in a uniform stream of velocity  $U_0$ . The classical approach to the analysis of such a flow field is to divide it into three regions, as shown in figure 1, in each of which a different set of approximations is made in the Navier-Stokes equations for laminar flow, and the corresponding Reynolds equations for turbulent flow. The resulting equations for the inviscid region 1 and the boundary-layer region 2 are well known. In the absence of flow reversal at the tail, the thick stern-flow boundary layer and the wake (region 3) can be described by the so-called partially-parabolic equations in which only streamwise gradients of the viscous and turbulent stresses are neglected. The interaction (or lack of one) between regions 1 and 2 is the classical problem of boundary-layer theory. In the present work, we are concerned with the flow in region 3 and its interaction with that in region 1.



There are two possible approaches to the solution of the partially-parabolic equations for region 3: a global approach in which one set of governing equations appropriate for both the inviscid- and viscous-flow regions is solved using a large solution domain (regions 3 and 1) so as to capture the entire zone of viscous-inviscid interaction; and an interactive approach in which different sets of governing equations are used for each region and the complete solution obtained through the use of an interaction law, i.e., patching or matching conditions. The former approach is somewhat more rigorous since it does not rely on the patching or matching conditions which usually involve further approximations. Nonetheless, for a variety of reasons, both types of approaches are of interest. In the present work, both are used in order to assess the accuracy of the interaction solution and highlight the essential differences between the two strategies, including their computational efficiency.

Besides the size of the solution domain, the primary difference between the two approaches lies in the conditions specified on the outer boundary  $S_0$  (see figure 1). For the noninteractive large-domain solutions, uniform-flow conditions are appropriate. The interactive solutions require the specification of the match boundary as well as an interaction law, and also a method for calculating the inviscid flow. In the previous work, solutions were obtained with the match boundary just beyond the thickness of the boundary layer  $\delta$ . In the present work, the influence of the location of the match boundary was investigated by obtaining solutions both with the match boundary just beyond  $\delta$  and with the match boundary at about  $2\delta$ . The interaction law is based on the concept of displacement thickness. The inviscid-flow solutions are obtained using a conforming-panel source-distribution method.

In the partially-parabolic equations, the velocity field is elliptic in transverse planes and parabolic in the streamwise direction while the pressure field is fully elliptic. Solutions to these equations can be obtained iteratively by solving the parabolic equations that result when the pressure field is specified and subsequently updating the pressure field using the results from the parabolic solutions. In the present approach, a body-fitted coordinate system, in which the axial coordinate is roughly aligned with the streamlines, is used. The partially-parabolic assumptions are made in this pre-

lected axial coordinate direction. Both numerical and analytic grid generation techniques are used. The governing equations are derived in nonorthogonal curvilinear coordinates with velocity components along the coordinate directions. The Reynolds stresses are modeled using the  $k-\epsilon$  turbulence model. The equations are discretized using finite differences and a staggered grid. The SIMPLER algorithm is used for velocity-pressure coupling. equations are solved implicitly by SOR by lines.

### III. EXTENSIONS FOR THREE-DIMENSIONAL FLOW

The methods described in Stern et al. (1986) are for general three-dimensional flow. However, during the course of the present calculations it was found that modifications of some of the finite-difference formulas were required. These are provided in Appendix II. The equation numbers used here correspond to those used previously in Appendix III of Stern et al. (1986). Referring to these Appendices, we note that the modifications involve moving certain terms from the source term to the main diagonal of the tridiagonal matrix formed when solving the  $y$ - and  $z$ -momentum equations and the turbulence model equations by SOR by lines.

Another departure from the previous procedures relates to the determination of the displacement thickness  $\delta^*(x,z)$ . An approximate method for determining  $\delta^*$  for three-dimensional bodies in terms of a local flux balance was outlined earlier. For the present applications to the simple elliptical cross-section bodies, an even more approximate procedure was used; that is, equation (V-11) of Stern et al. (1986) was used to determine the displacement thicknesses along only the major and minor axes, and these were connected under the assumption that the displacement body is also elliptic in cross section.

### IV. APPLICATIONS TO THREE-DIMENSIONAL BODIES

#### A. Elliptical Cross-Section Bodies

The two calculation schemes were applied to two simple three-dimensional bodies: namely, the DTNSRDC 2:1 and 3:1 elliptical cross-section bodies for which experimental data have been obtained by Huang and associates (Groves et

al., 1982; Huang et al., 1983 and 1985). Figure 2 shows a schematic view of the bodies. These bodies have the same length and longitudinal distribution of cross-sectional area as the Afterbody 1 for which results were presented in the previous report.

## B. Calculations

The calculations for both bodies were performed for a body-length Reynolds number  $R_n = 6.5 \times 10^6$  which corresponds to the experimental conditions. Typical large- and small-domain grids used in the calculations are shown in figures 3 and 4 for the 2:1 and 3:1 bodies, respectively. Figures 3a,b and 4a,b show the grids in the minor axis plane while figures 3c,d and 4c,d show the cross-sectional views at  $X = .8966$ . For the 2:1 body, the large-domain grid was obtained using a numerical technique through the solution of elliptic partial differential equations whereas the small-domain grid was constructed using an analytic technique in which grids for each cross section were pieced together (stacked) in the streamwise direction. For the 3:1 body, both the large- and small-domain grids were obtained using the numerical technique. In this case, the difference between the two grids is that the small-domain grid was obtained simply by deleting that portion of the large-domain grid which lay beyond about two boundary-layer thicknesses. This was done to evaluate the accuracy of the two approaches and to determine the effects of the placement of the outer boundary in the interaction solution.

Referring to figures 1 and 3a,c for notation, for the 2:1 body large-domain solutions, there are 55, 18, and 5 grid points in the axial, radial, and girthwise directions, respectively. The solution domain is bounded by the inlet  $S_I$  at  $x_u = .5$ , the exit  $S_E$  at  $x_d = 2.5$ , the outer boundary at  $y_o = 1.05$ , the body surface, and the two planes of symmetry ( $\theta = 0^\circ$  and  $90^\circ$ ). The first grid point off the body surface was located in the range  $150 < y^+ < 300$ . Referring to figures 1 and 3b,d, for the small-domain solutions, there are 55, 15, and 5 grid points. The inlet and exit boundaries as well as the first grid point off the body surface have the same values as in the large-domain grid, but the outer boundary is now placed at  $y_o = \delta$ , where  $\delta(x,z)$  is the boundary layer thickness which was specified from the experimental results. In both cases, the grid expansion was specified such that the first two grid

points lie in the log-law region. For the 3:1 body (figures 1 and 4), the number of grid points and boundary values, including the location of the first grid point off the body surface, are similar to those in the large-domain grid for the 2:1 body. The difference between the large- (figures 4a,c) and small-domain (figures 4b,d) grids for the 3:1 body is that in the former 19 radial grid points were used whereas in the latter only 11 were used. This places the outer boundary in the interaction solution at about twice the boundary-layer thickness.

For both applications standard turbulent flat-plate profiles were used to specify the initial conditions. All other boundary conditions were prescribed as discussed in Section IV.D of Stern et al. (1986). The calculations were performed on a Prime 9950 minicomputer. An underrelaxation factor  $\alpha_p$  was used in solving the pressure equation. For the large-domain solutions  $\alpha_p = .2-.4$  whereas for the interaction solutions  $\alpha_p = .3-.4$ . The large-domain solution for the 2:1 body converged in 40 iterations and required 120 minutes of cpu time, and for the 3:1 body, it converged in 45 iterations and required 135 minutes of cpu time. The interaction solutions converged in 30 iterations and required 90 minutes of cpu time in both cases.

### C. Results and Discussion

The results for the 2:1 body are presented in figures 5 through 13 and those for the 3:1 body in figures 14 through 22. First, the convergence history of both approaches is considered. Figures 5 and 6 show the convergence histories with regard to the pressure distribution for the 2:1 body for the large-domain and interaction solutions, respectively. For the former, values are shown for every 10 global iterations, whereas for the latter, values are shown after every 5 global iterations. Figure 7 shows the convergence history of the displacement thickness for the interaction solution. Corresponding results for the 3:1 body are shown in figures 14 through 16. The interaction solutions were started with free-stream edge conditions ( $U_e = 1.$ ,  $W_e = 0.$ ,  $p_e = 0$ ). After 15 iterations for the 2:1 body and 20 iterations for the 3:1 body, the edge conditions were updated using the latest displacement thickness. Subsequent updates of the edge conditions were not made. Note that for Afterbody 1 it was shown that small changes in displacement body

after intermediate convergence was achieved (circa. 15-20 iterations), led to insignificant changes in the edge conditions. This was also confirmed for the present applications through numerical experimentation. The magnitude of the edge velocity  $Q_e = \sqrt{1-C_p}$  used in the interaction solutions is shown in figures 8 and 17 for the 2:1 and 3:1 bodies, respectively. As was the case for axisymmetric flow and discussed with reference to figures 27 and 28 of Stern et al. (1986), the two solutions show quite different convergence characteristics. The large-domain solutions converge monotonically in about 40 to 45 iterations for both bodies, whereas the interaction solutions converge with oscillations in about 30 iterations and with two stages (for both cases). The first stage is with free-stream edge conditions and leads to an underprediction of both  $C_p$  and  $\delta^*$ . The second stage is with the displacement-body edge conditions and the solutions converge quite rapidly. Figures 9 and 18 show the final values of displacement thickness for the interaction solutions for  $\theta = 0^\circ$  and  $90^\circ$  for the 2:1 and 3:1 bodies, respectively. Note that, in both cases, the displacement thickness is larger along  $\theta = 90^\circ$  than along  $\theta = 0^\circ$  leading to stronger viscous-inviscid interaction along  $\theta = 90^\circ$ .

Next, a comparison is made between the two solutions and also the experimental data. Figure 10 shows the pressure distribution on the surface of the body and along the wake centerline for the 2:1 body for three girthwise positions  $\theta = (0^\circ, 80^\circ, 90^\circ)$ ,  $\theta = 0^\circ$  corresponding to the waterplane (minor axis) symmetry plane and  $\theta = 90^\circ$  to the keel (major axis) symmetry plane (see figure 2). The converged results from the two methods, i.e., the noninteractive large-domain solutions and the small-domain viscous-inviscid interaction solutions, are compared with the experimental data and the inviscid-flow solution without interaction. It is seen that both methods are in good agreement with the experimental data. However, just as was the case for the axisymmetric bodies, the interaction solution is in slightly better agreement. This is due to the influence of the initial conditions and the better grid resolution within the boundary-layer region for the interaction solution. The degree of viscous-inviscid interaction due to the stern boundary layer and wake for this body is similar in magnitude to that for the parent axisymmetric shape (Afterbody 1). Also, note the larger viscous effects along  $\theta = 90^\circ$  than along  $\theta = 0^\circ$ . Figure 11 shows the girthwise pressure

distribution at several axial stations. Consistent with figure 10, the interaction solution shows better agreement with the experimental data. The increase in pressure towards  $\theta = 90^\circ$  is expected due to the rapid change of body curvature in this region. The results for the 3:1 body corresponding to figures 10 and 11 are shown in figures 19 and 20. It is seen that the viscous-inviscid interaction is larger for the 3:1 body than it is for the 2:1 body, especially near the keel. The differences between the large-domain and interaction solutions for the 3:1 body are less pronounced than those for the 2:1 body and previously for axisymmetric bodies. This is no doubt due to the fact that for the 3:1 body both methods have the same number and distributions of radial grid points within the viscous-flow region. The comparison with the experimental data is not as good as shown for the 2:1 body.

The calculated distributions of the wall-shear velocity  $U_\tau$  along three girthwise positions ( $\theta = 0^\circ, 77^\circ, 90^\circ$ ) on the 2:1 body are compared with the experimental values deduced from Preston tubes in figure 12. In this case, the agreement between the two sets of calculations is good but the experimental values are lower especially in the region  $X > 0.9$ . This discrepancy could be attributed to deficiencies of the turbulence model; however, as noted by Chen and Patel (1985) from a reanalysis of the data, the  $U_\tau$  values deduced from the measured velocity profiles and Clauser plots are higher and are in better agreement with the calculations. The corresponding results for the 3:1 body are shown in figure 21. Consistent with the earlier discussion, the two solutions are in even closer agreement than that in the case of the 2:1 body. Unfortunately, experimental values are not quoted to verify the results.

Figure 13 shows the profiles of  $(U, V, W, C_p, k, \epsilon)$  for the 2:1 body at five stations on the body  $X = (.767, .894, .914, .944, .956)$  where experimental data is available (see figure 2). In these figures, the radial coordinate is defined as  $Y = (R - R_0)/R_{\max}$  where  $R_0(x)$  is the local body radius,  $R$  is the distance from the body surface along the local normal to the body cross section, and  $R_{\max}$  is the maximum value of the geometrical mean radius (i.e., the maximum radius of the Afterbody 1). The calculated velocity components have been interpolated and transformed into the experimental coordinate system in order to make the comparisons. The  $U$  component is in the axial cartesian

coordinate direction, the  $V$  component is in the direction of the local normal to the body cross section, and the  $W$  component is orthogonal to both  $U$  and  $V$ . Consistent with the results discussed above, both solutions are in good agreement; however, some differences are evident, especially in the pressure. That is, while both solutions indicate similar transverse pressure gradients  $p_y$  there are systematic differences in pressure magnitude. The large-domain solution predicts lower pressure than the interaction solution which, in general, shows better agreement with the experimental data. A similar trend was found previously in the results for axisymmetric bodies. This may be related to the outer boundary conditions in the large-domain solution since its characteristics are similar to a blockage effect. The velocity components are in good agreement with the experimental data. This is especially true for the  $U$  component. The  $V$  component is slightly over predicted. The  $W$  component is quite small and difficult to compare with the experimental values. Actually, the experimental  $W$  values indicate an error in the alignment of the model since nonzero values are shown for the symmetry planes,  $\theta = 0^\circ$  and  $90^\circ$ . The calculations show a systematic overprediction of the turbulent kinetic energy as the boundary layer thickens; namely, as the tail is approached and increasingly so towards  $\theta = 90^\circ$ . This is undoubtedly due to deficiencies of the turbulence model.

Corresponding results for the 3:1 body are shown in figure 22. In this case, the body station values are  $X = (.719, .810, .894, .934, .954)$  (see figure 2). Here again, the two solutions are in even closer agreement than that shown for the 2:1 body; however, a difference in pressure magnitude is still evident. The level of agreement with the experimental data for the symmetry planes (i.e.,  $\theta = 0^\circ$  and  $90^\circ$ ) is very good and similar to that shown previously for the 2:1 body. However, the results for  $\theta = 80^\circ$  do not show overall good agreement with the experimental data. The  $U$  component shows a discrepancy that begins in the outer part of the boundary layer at  $X = .81$  and becomes progressively worse and encompasses more of the boundary layer as the tail is approached. The  $V$  component is overpredicted, the  $W$  component indicates negative values whereas the experimental values are positive, and the turbulent kinetic energy is overpredicted. A similar discrepancy in the  $U$  component occurs in the outer part of the boundary layer in the previous

results for the 2:1 body and Afterbody 5; however, in these cases it is confined to the outer part of the boundary layer and the error is small. Further numerical testing is required, including grid refinement and comparisons with more extensive sets of experimental data, in order to determine the cause.

## V. CONCLUDING REMARKS

A viscous-inviscid interaction method for three-dimensional flows which require higher-order viscous-flow equations, has been validated by comparisons with experimental data for two simple three-dimensional bodies; namely, the DTNSRDC 2:1 and 3:1 elliptical cross-section bodies. The relative merits of interactive and global solution procedures were evaluated by comparing the interaction solutions with the large-domain solutions of only the viscous-flow equations. Both methods yield similar results in good general agreement with the data. The level of agreement between the two approaches and with the experimental data is similar to that shown previously for axisymmetric bodies.

As was anticipated on the basis of previous calculations for axisymmetric bodies, the interaction solution is computationally more efficient than the large-domain solution, i.e., 25% savings in overall cpu time for the cases considered. This is due to the fact that the prescription of the inviscid-flow at the boundary-layer edge accelerates the convergence of the viscous-flow solution. Although there is an additional computational effort in calculating the inviscid flow, the savings in the calculation of the viscous-flow is more substantial.

The feasibility of both the present approaches has now been demonstrated for various levels of flow field complexity: two-dimensional, axisymmetric, and simple three-dimensional bodies. The results are quite satisfactory and warrant further work in extending the present procedures for more realistic ship geometries and complex flow fields. Of particular interest, is the extension of the interaction approach for the calculation of ship boundary layers and wakes, including the effects of free-surface waves, i.e., for non-zero Froude numbers, by coupling the present viscous-flow method with a potential-flow solution procedure, such as Dawson's method (1977), in a similar manner as has been done presently for zero Froude number. It is believed that an interaction approach is more readily extendible to the problem of calculating ship boundary layers at nonzero Froude numbers.



## REFERENCES

Chen, H.C. and Patel, V.C., (1985), "Calculation of Trailing Edge, Stern and Wake Flows by a Time-Marching Solution of the Partially-Parabolic Equations", Iowa Institute of Hydraulic Research, University of Iowa, IIHR Report 285.

Dawson, C.W., (1977), "A Practical Computer Method for Solving Ship-Wave Problems", Proc. 2nd Int. Conf. on Numerical Ship Hydrodynamics, Berkeley, CA, pp. 30-38.

Groves, N.C., Belt, G.S. and Huang, T.T., (1982), "Stern Boundary-Layer Flow on a Three-Dimensional Body of 3:1 Elliptic Cross Section", DTNSRDC Rept. 82/022.

Huang, T.T., Groves, N.C. and Belt, G.S., (1983), "Stern Boundary-Layer Flow on Two Three-Dimensional Bodies Having Elliptical Transverse Cross-Sections", 2nd Sym. on Numerical and Physical Aspects of Aerodynamic Flows, Long Beach, CA.

Huang, T.T., Groves, N.C. and Belt, G.S., (1984), "Stern Boundary-Layer Flow on a Three-Dimensional Body of 2:1 Elliptic Cross Section", DTNSRDC Rept. 84/022.

Stern, F., Yoo, S.Y. and Patel, V.C., (1986), "Viscous-Inviscid Interaction With Higher-Order Viscous-Flow Equations", Iowa Institute of Hydraulic Research, University of Iowa, IIHR Report 304. Also, "Interactive and Large-Domain Solutions of Higher-Order Viscous-Flow Equations", submitted to the AIAA Journal.

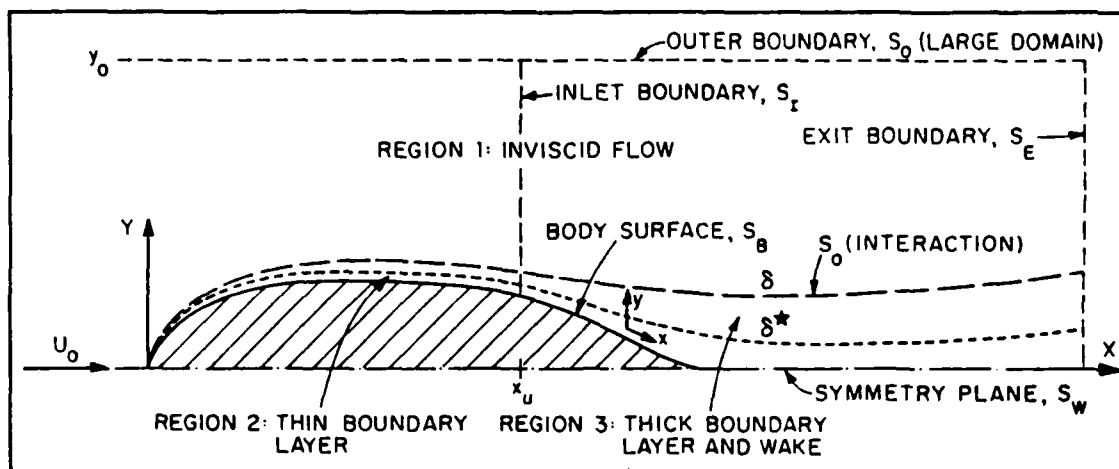


Figure 1a. (X,Y) Plane

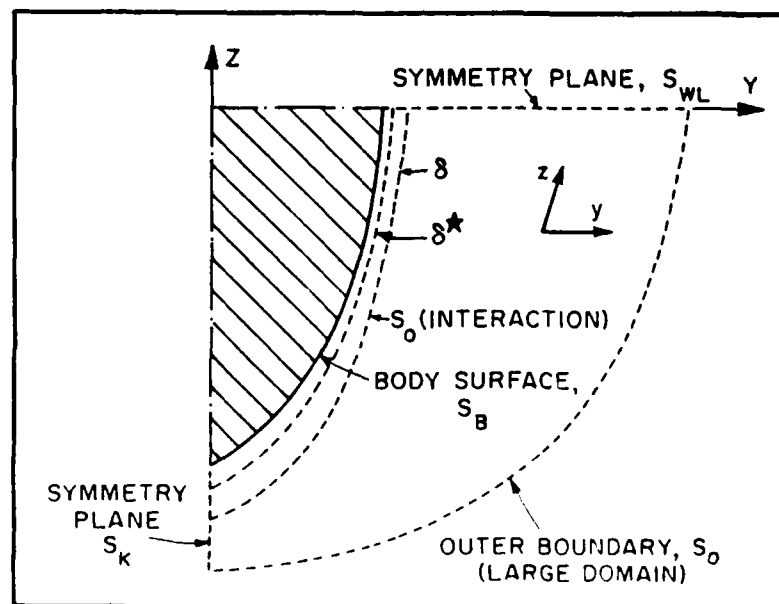


Figure 1b. (Y,Z) Plane

Figure 1. Definition Sketch of Flow-Field Regions.

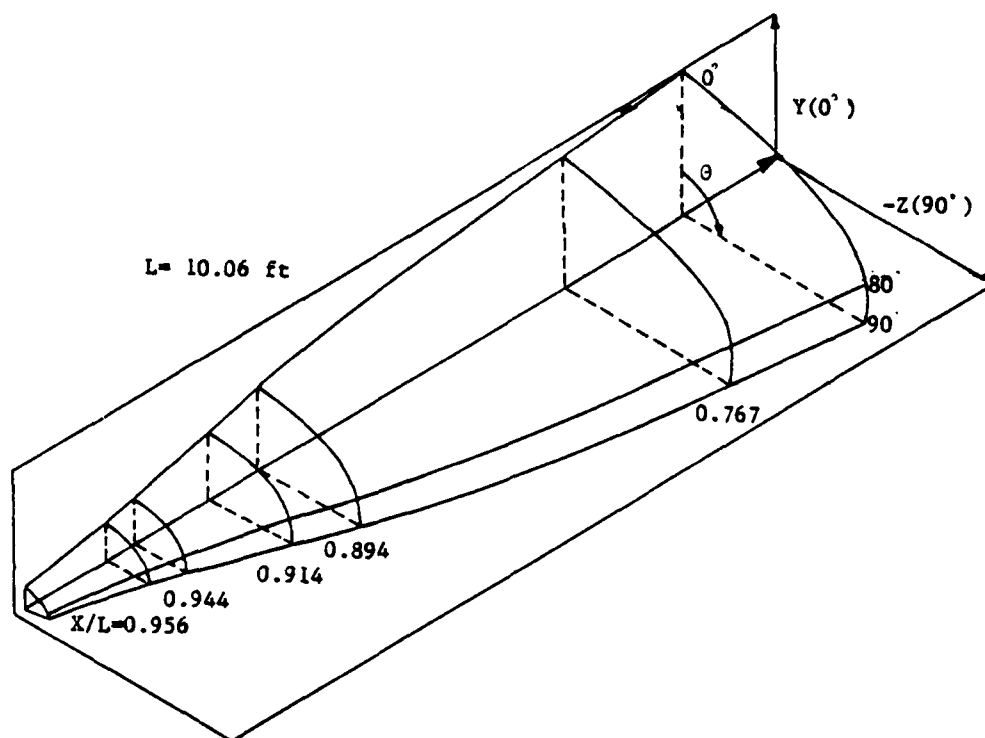


Figure 2a. 2:1 Body

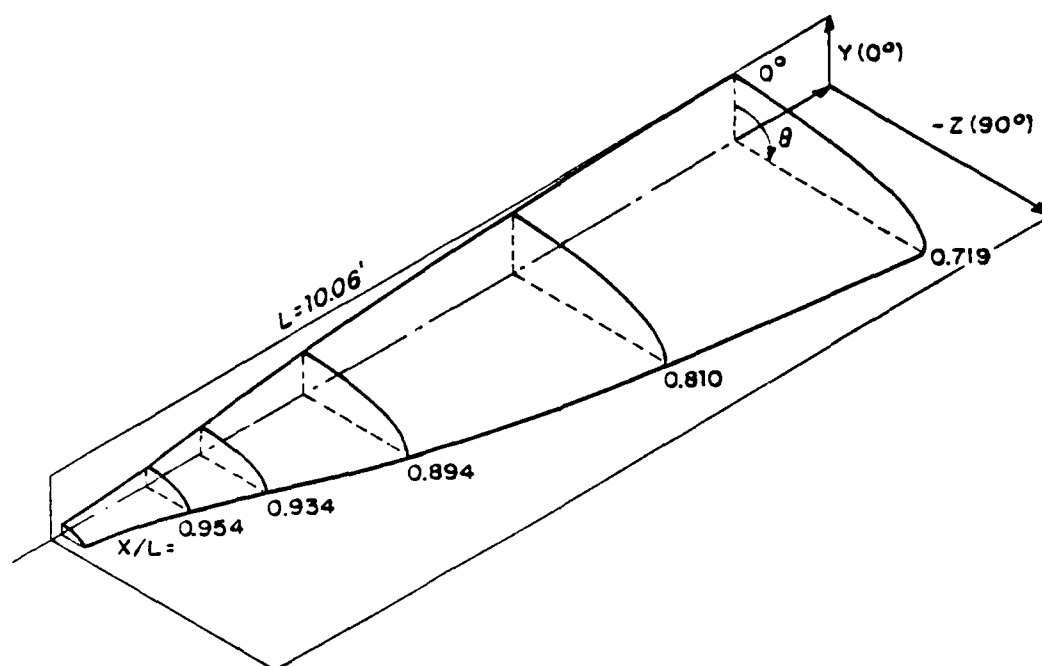


Figure 2b. 3:1 Body

Figure 2. DTNSRDC Elliptical Cross-Section Bodies.

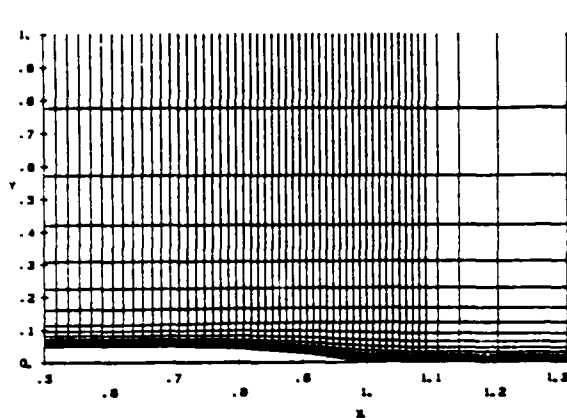


Figure 3a. Large-Domain Grid: Minor Axis Plane (Partial View)

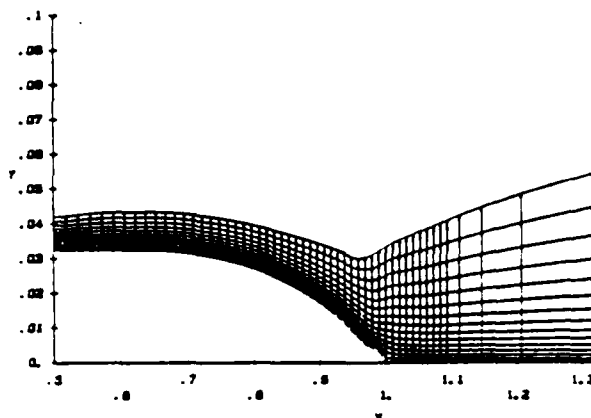


Figure 3b. Small-Domain Grid: Minor Axis Plane (Partial View)

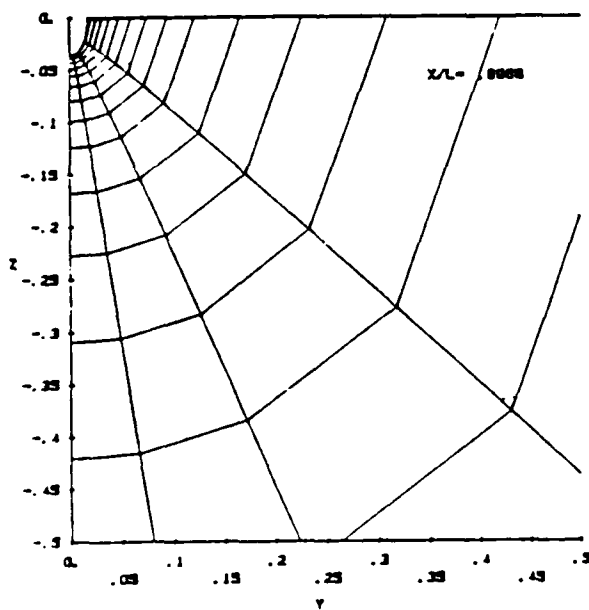


Figure 3c. Large-Domain Grid: Cross-Sectional Plane (Partial View)

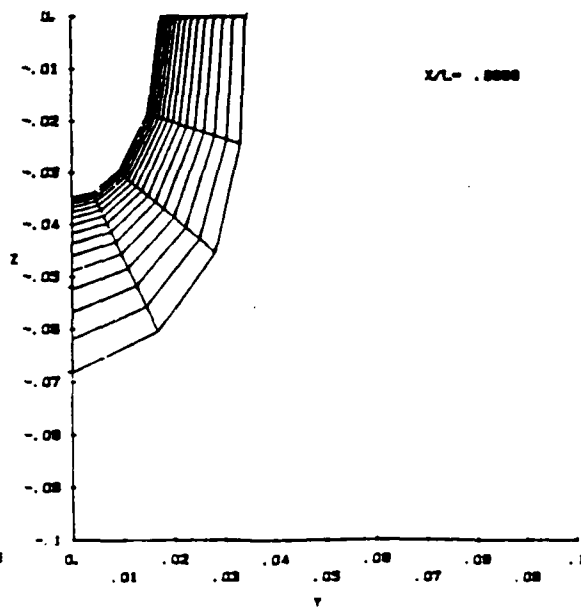


Figure 3d. Small-Domain Grid: Cross-Sectional Plane

Figure 3. Grids for the 2:1 Body.

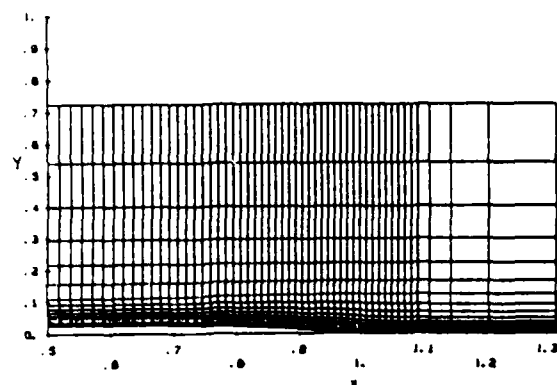


Figure 4a. Large-Domain Grid: Minor Axis Plane (Partial View)

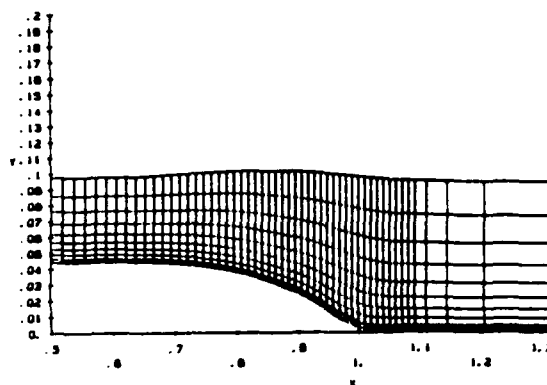


Figure 4b. Small-Domain Grid: Minor Axis Plane (Partial View)

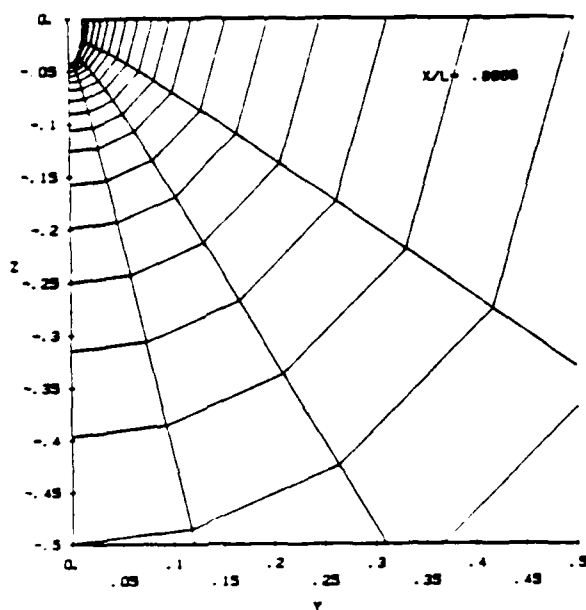


Figure 4c. Large-Domain Grid: Cross-Sectional Plane (Partial View)

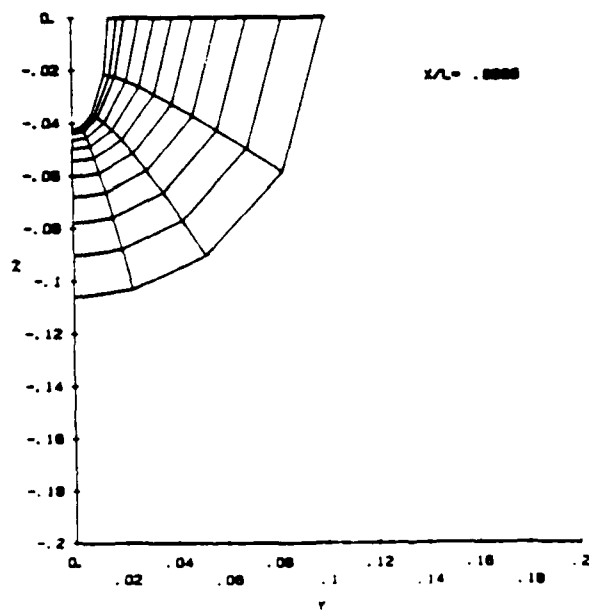


Figure 4d. Small-Domain Grid: Cross-Sectional Plane

Figure 4. Grids for the 3:1 Body.

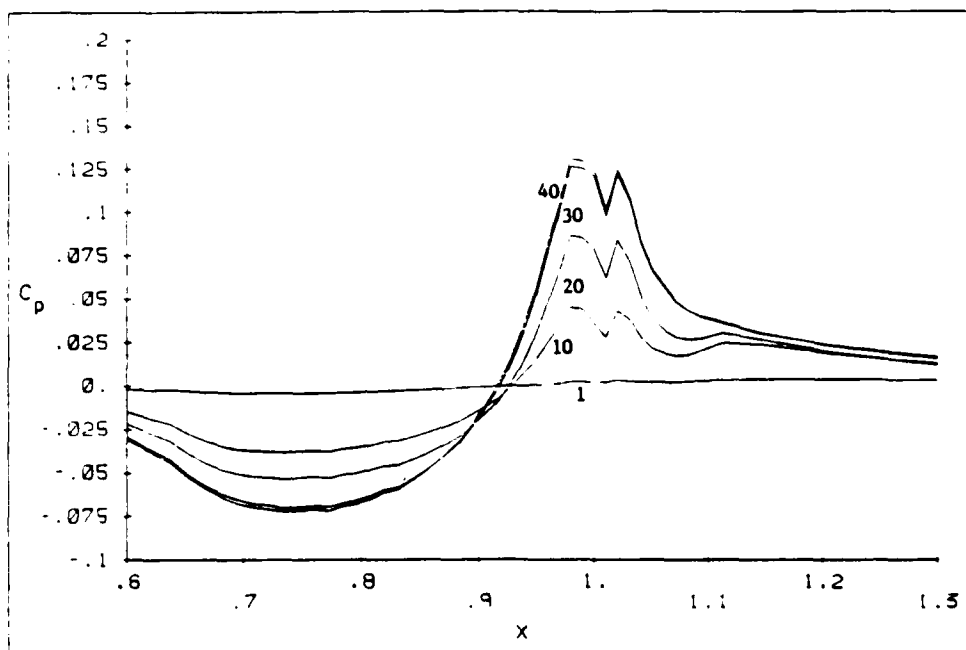


Figure 5. Convergence History of the Pressure Distribution on the Surface of the Body and Along the Wake Centerline: Minor Axis Plane, Large-Domain Solution.

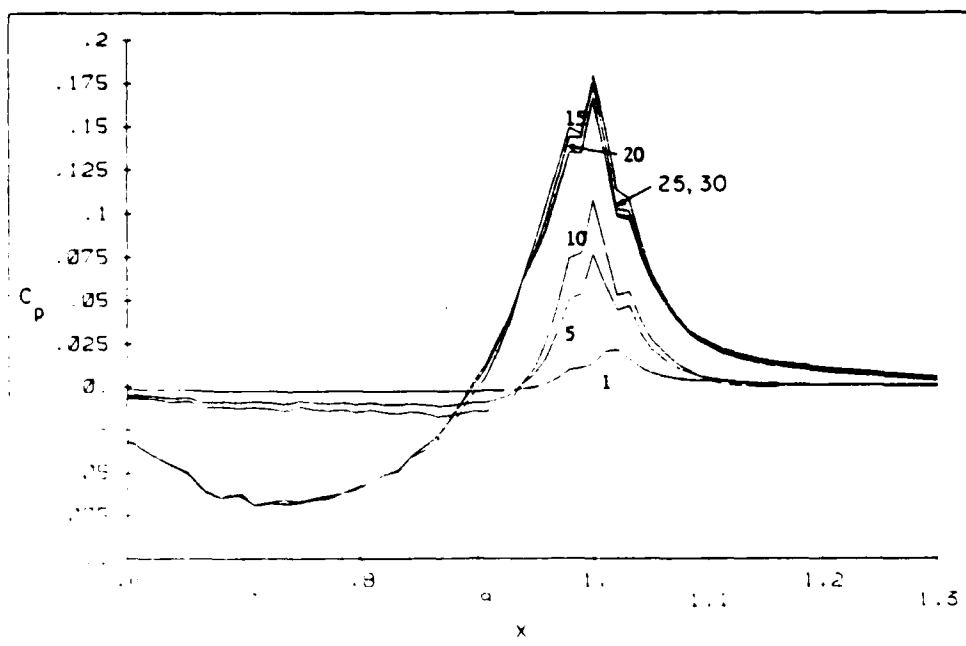


Figure 6. Convergence History of the Pressure Distribution on the Surface of the Body and Along the Wake Centerline: Minor Axis Plane, Interaction Solution.

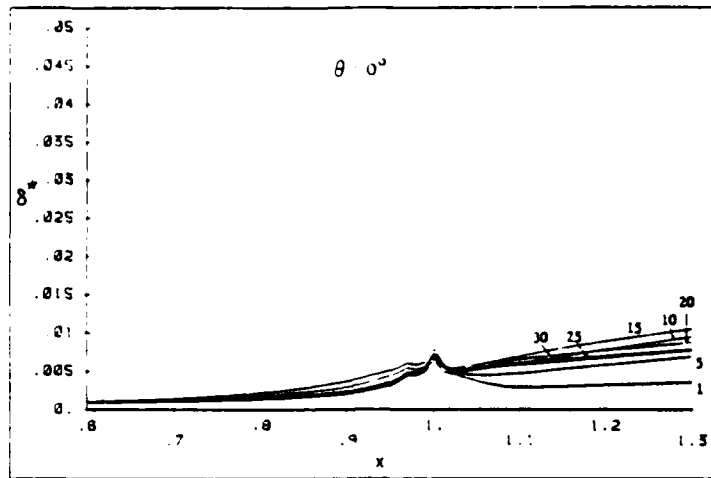


Figure 7. Convergence History of the Displacement Thickness: Minor Axis Plane, Interaction Solution.

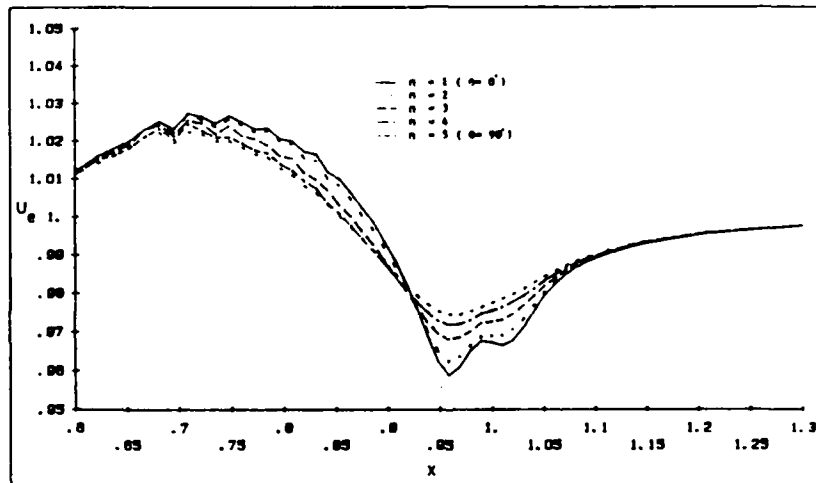


Figure 8. Edge Velocity.

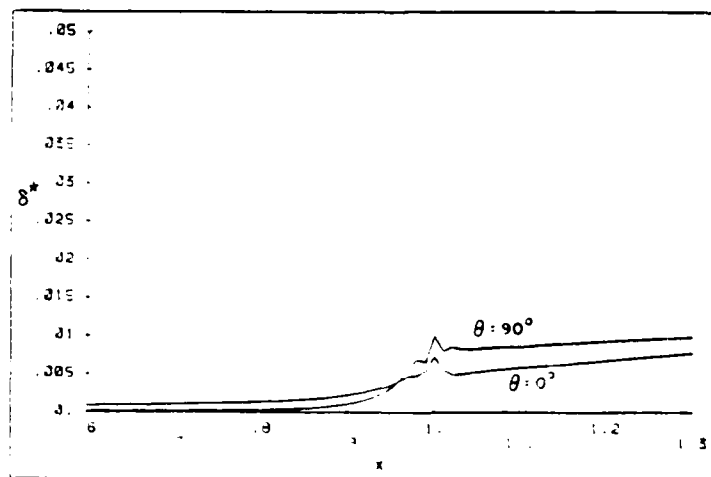


Figure 9. Displacement Thickness: Minor and Major Axes Planes, Interaction Solution.

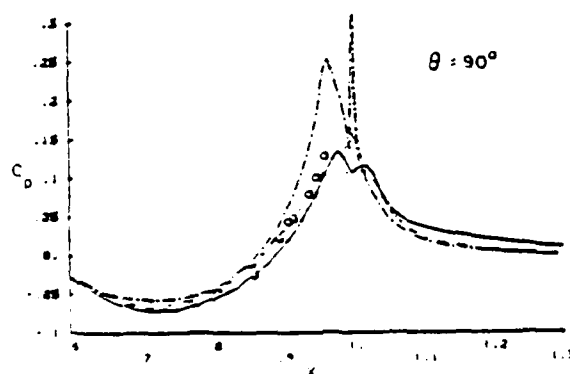
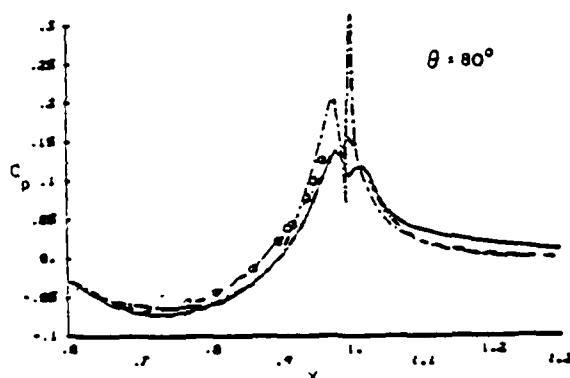
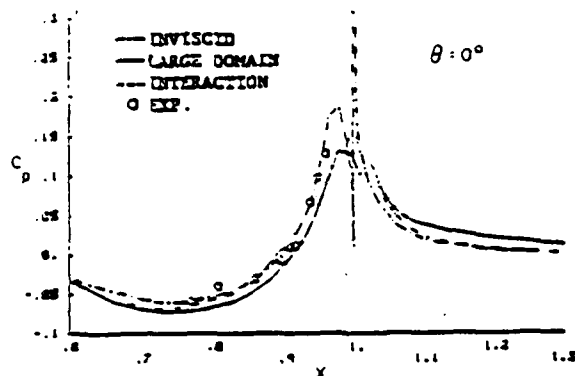


Figure 10. Pressure Distribution on the Surface of the Body and Along the Wake Centerline.

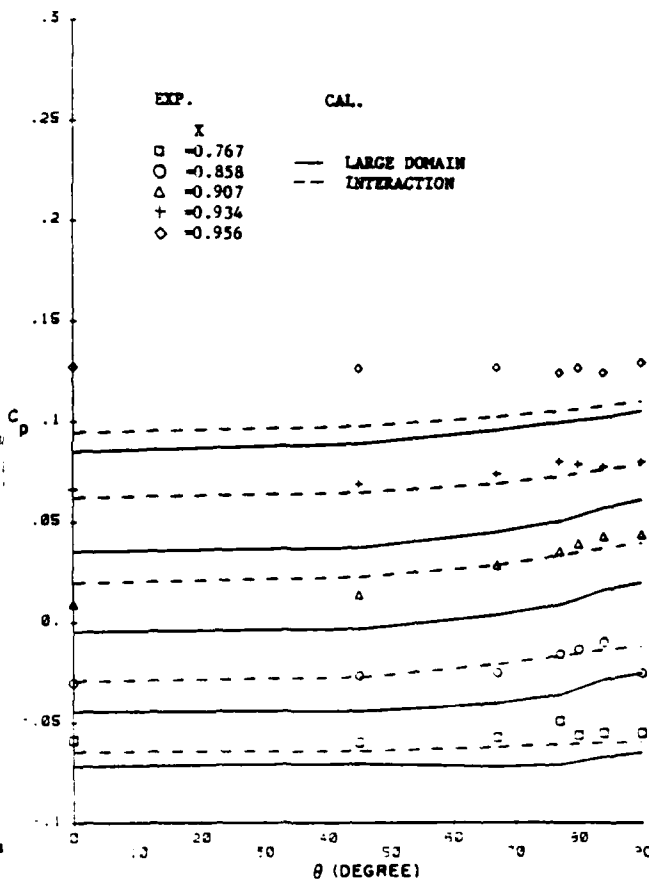


Figure 11. Girthwise Variation of Pressure on the 2:1 Body.



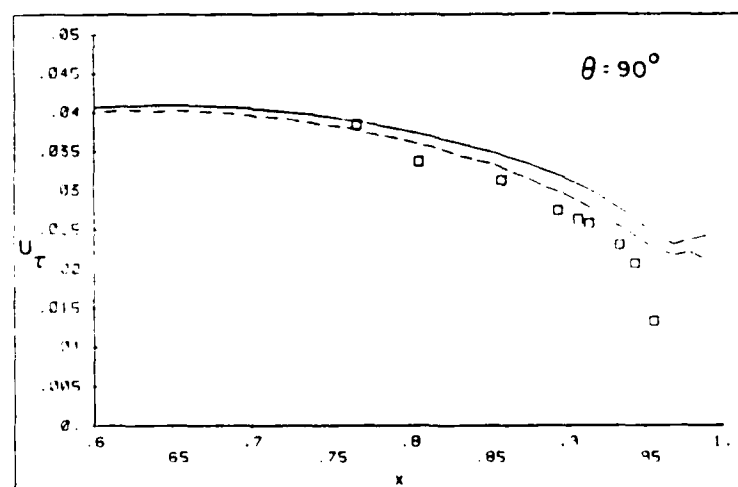
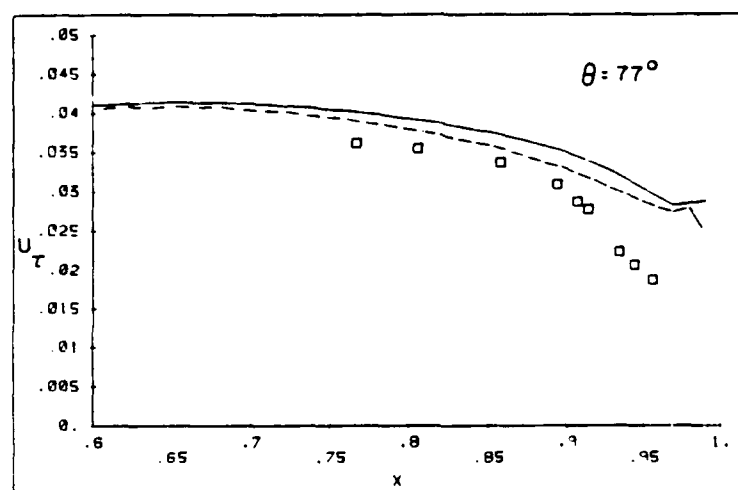
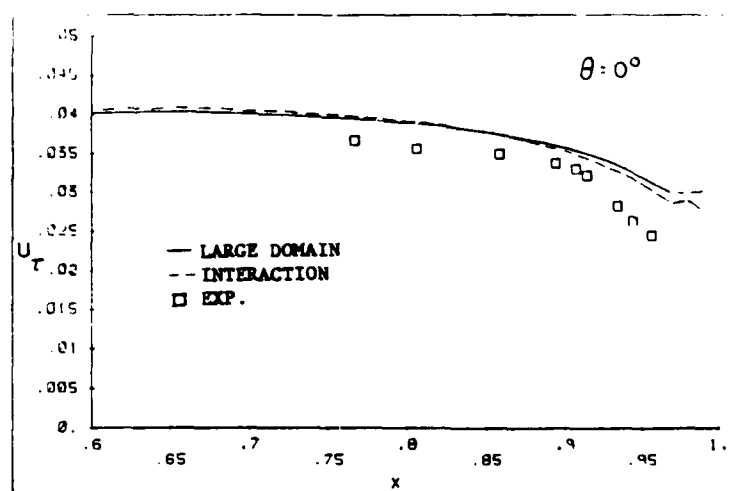


Figure 12. Wall-Shear Velocity.

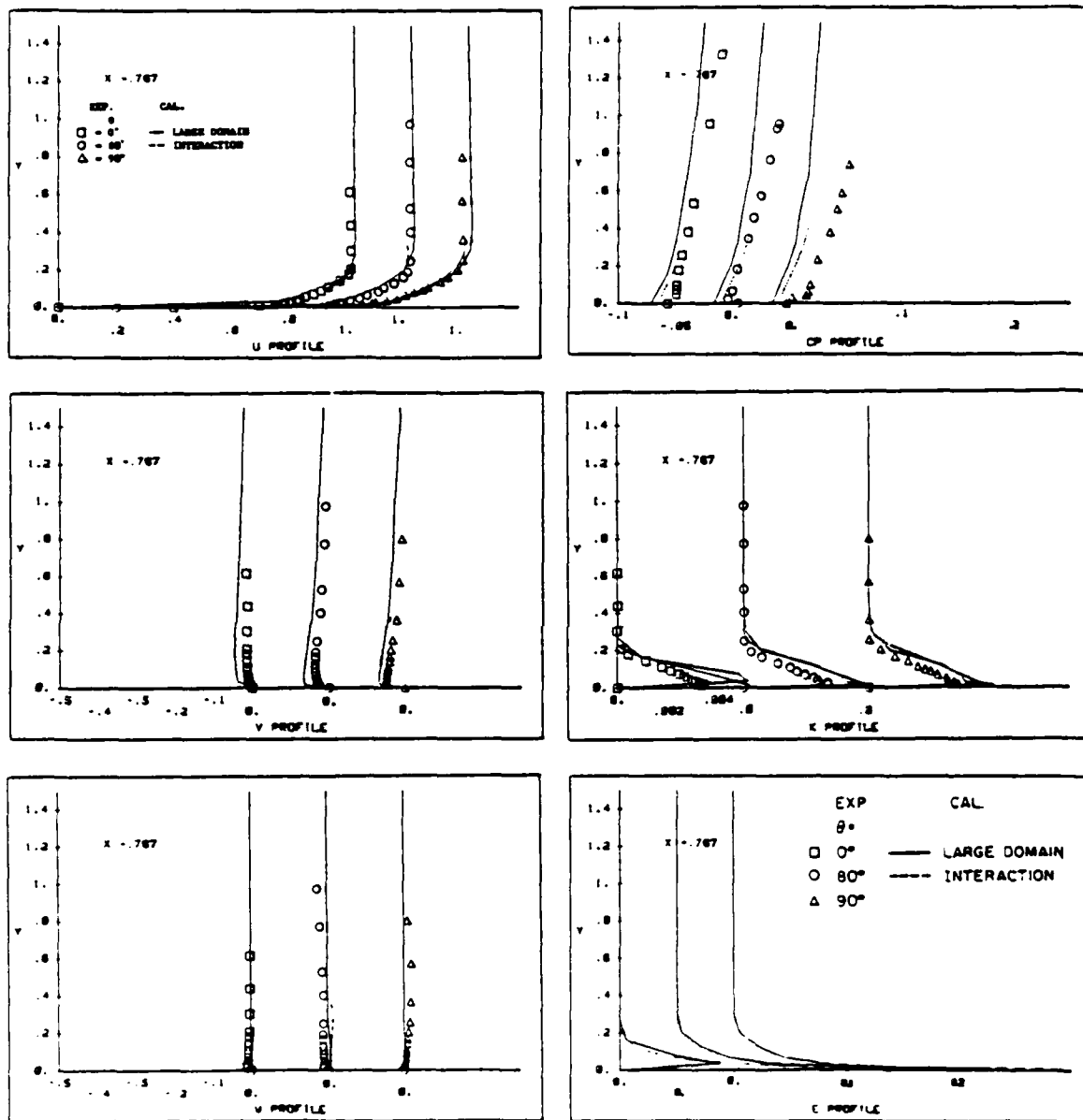


Figure 13. Solution Profiles.

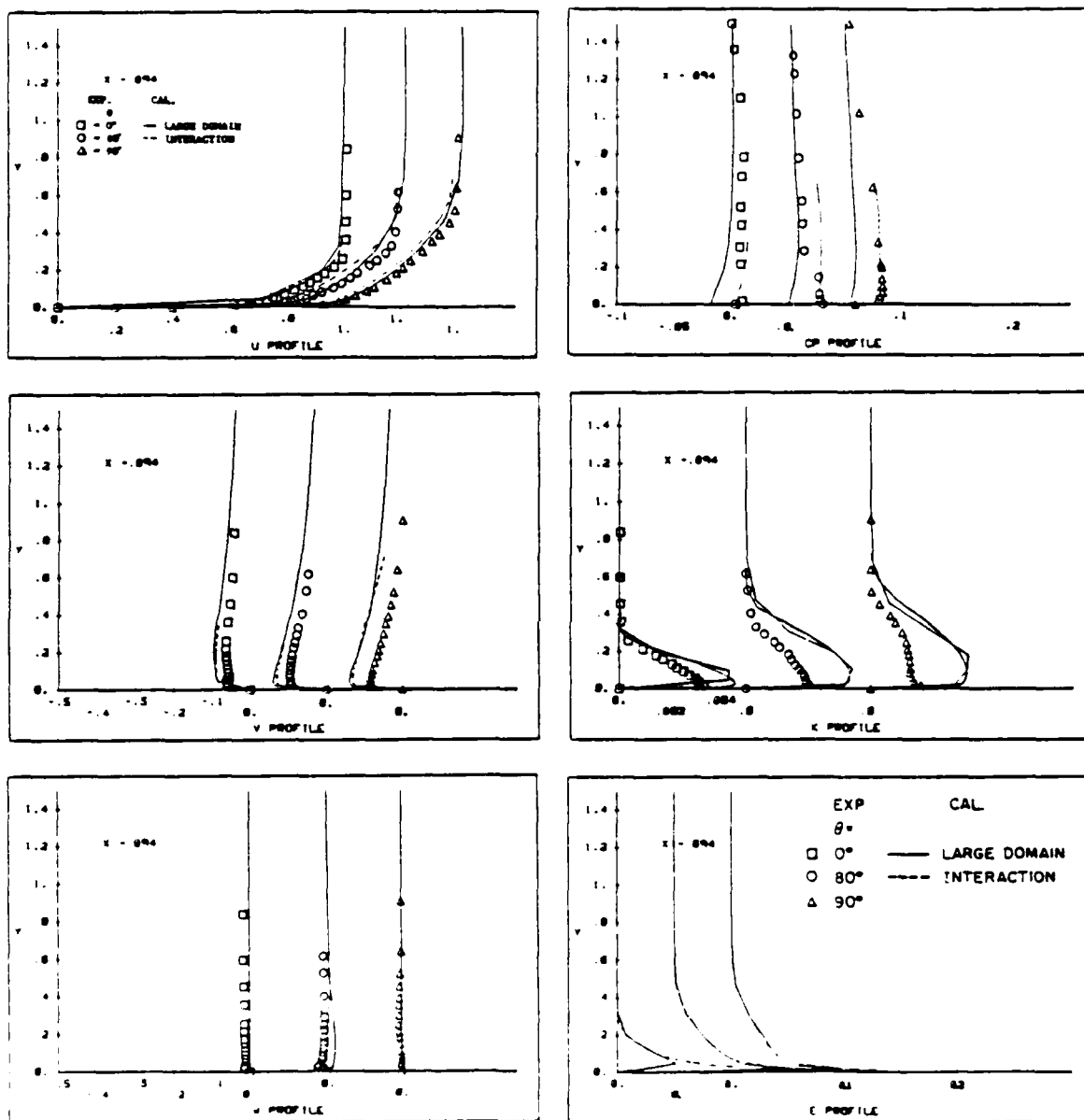


Figure 13. (Continued).

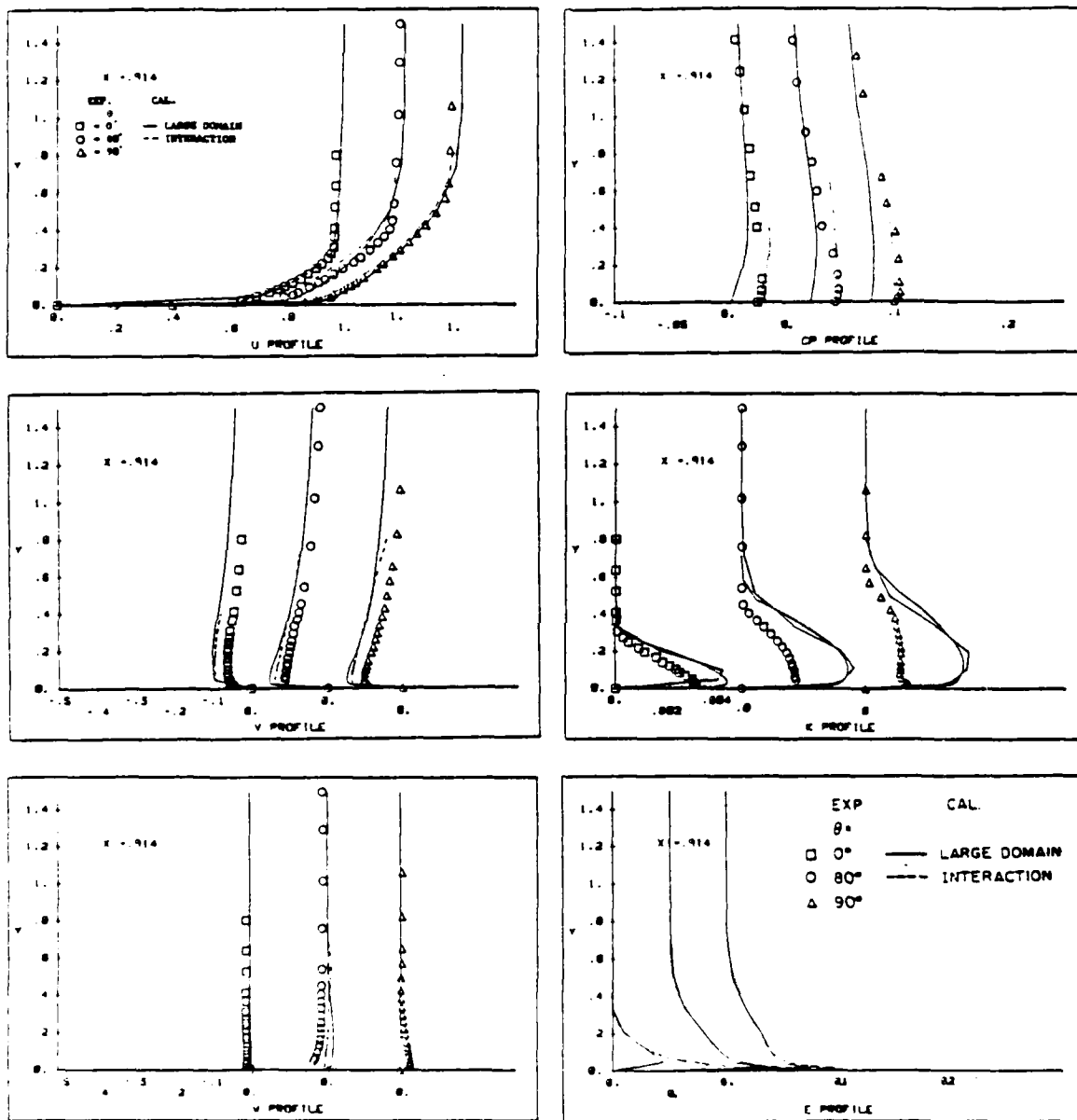


Figure 13. (Continued).

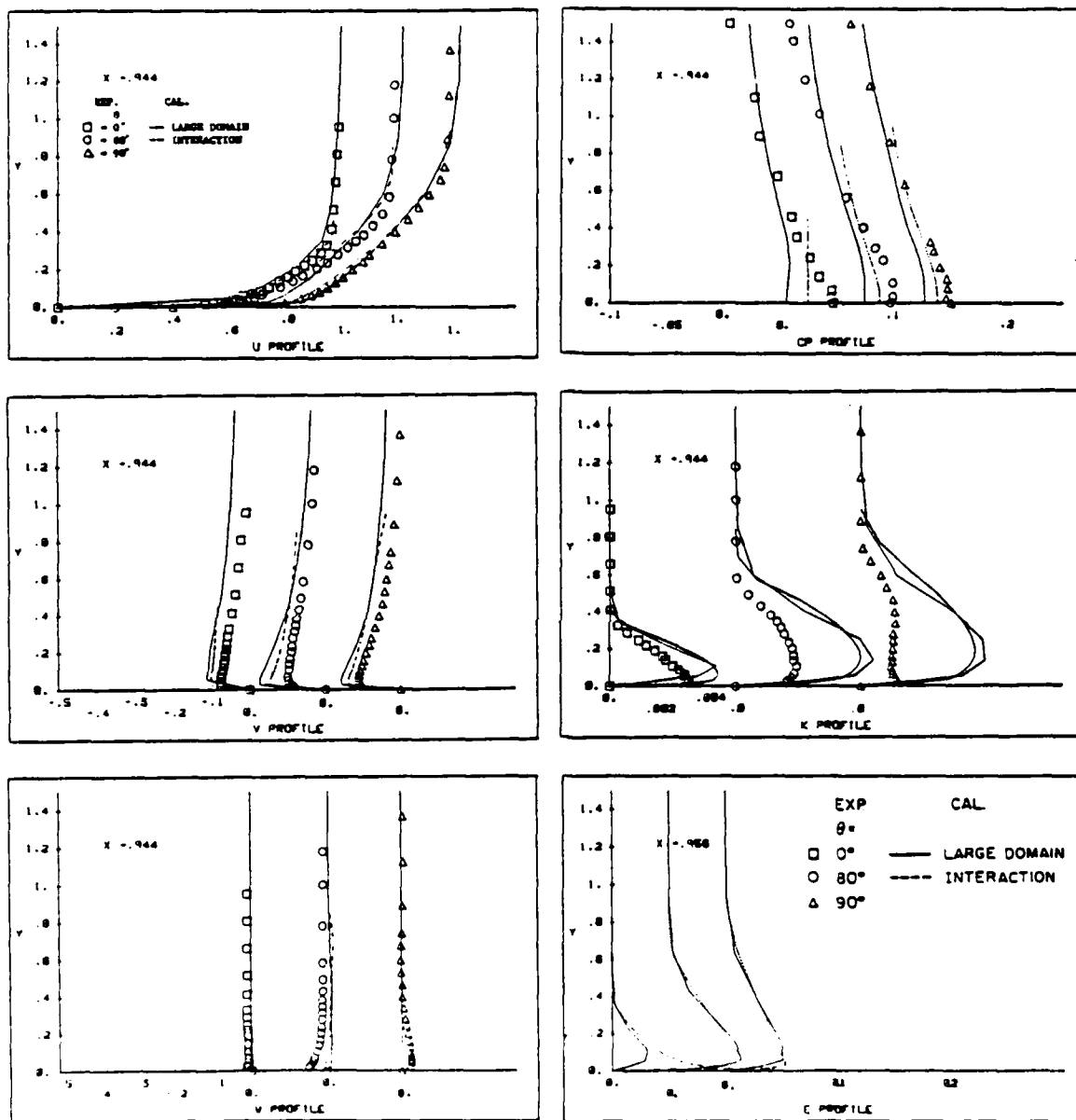


Figure 13. (Continued).

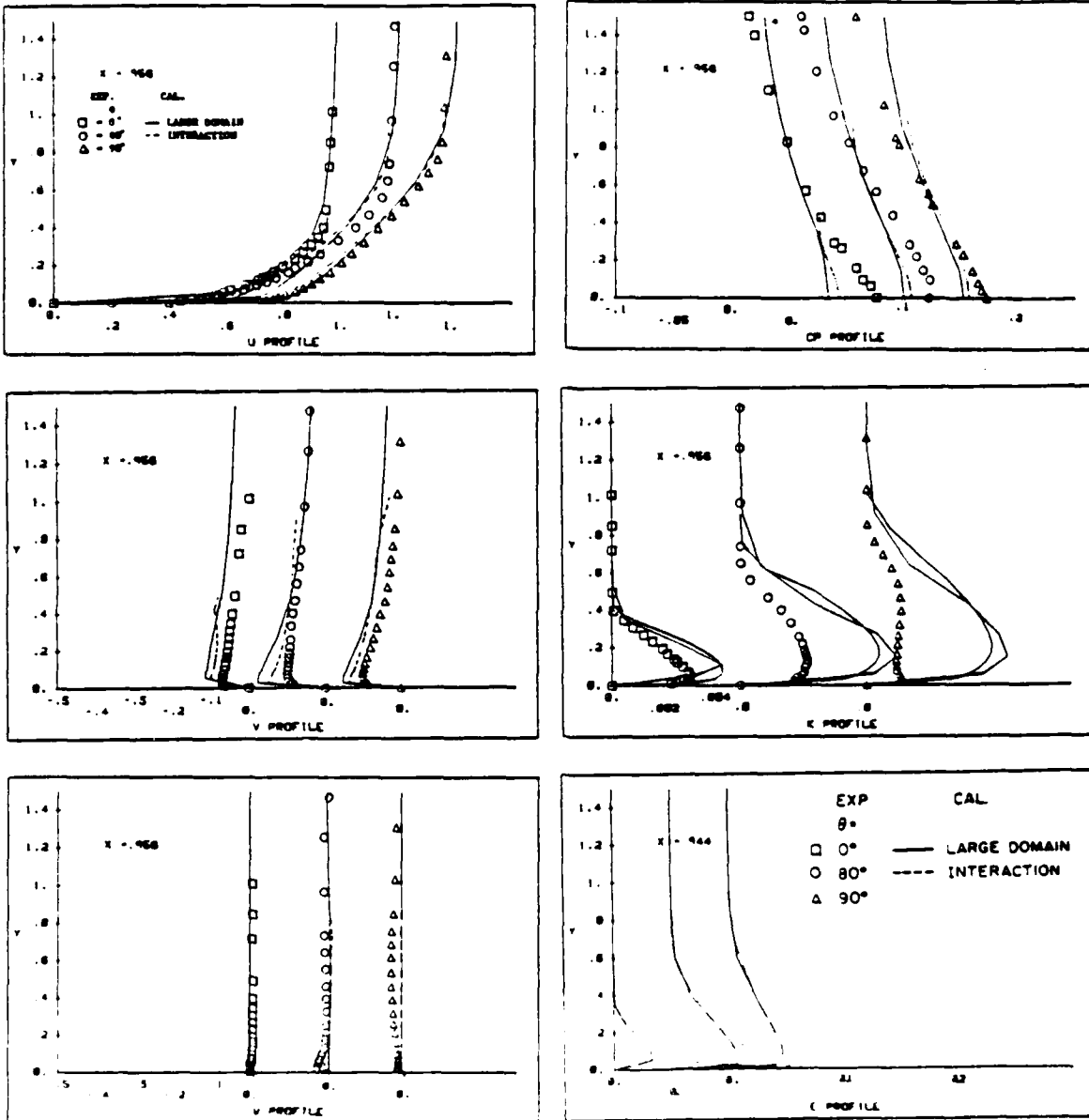


Figure 13. (Continued).

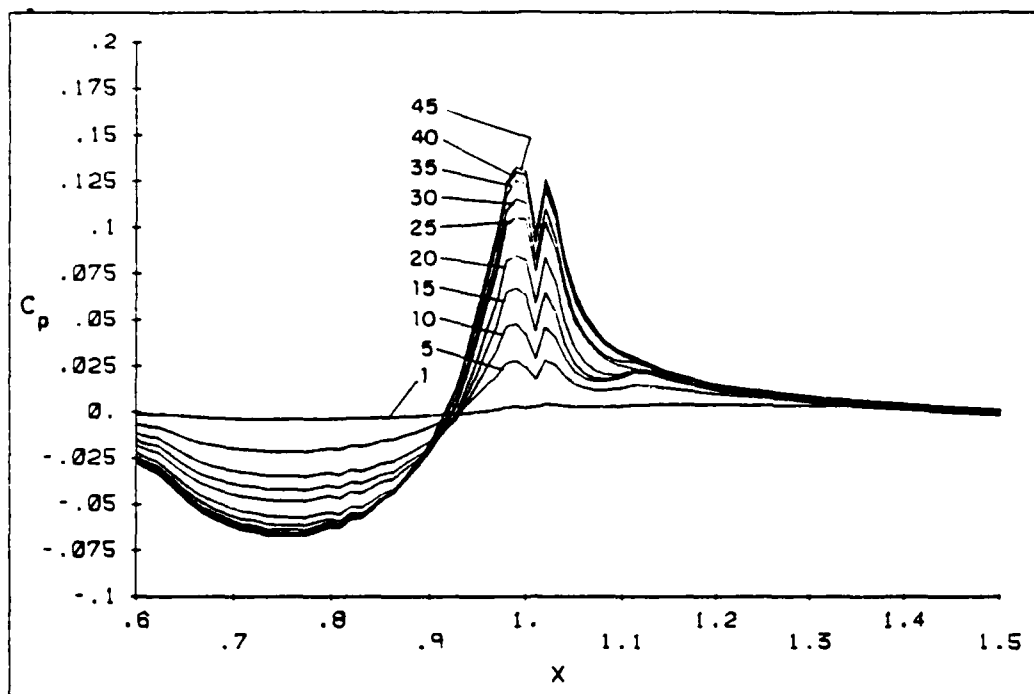


Figure 14. Convergence History of the Pressure Distribution on the Surface of the Body and Along the Wake Centerline Minor Axis Plane, Large-Domain Solution

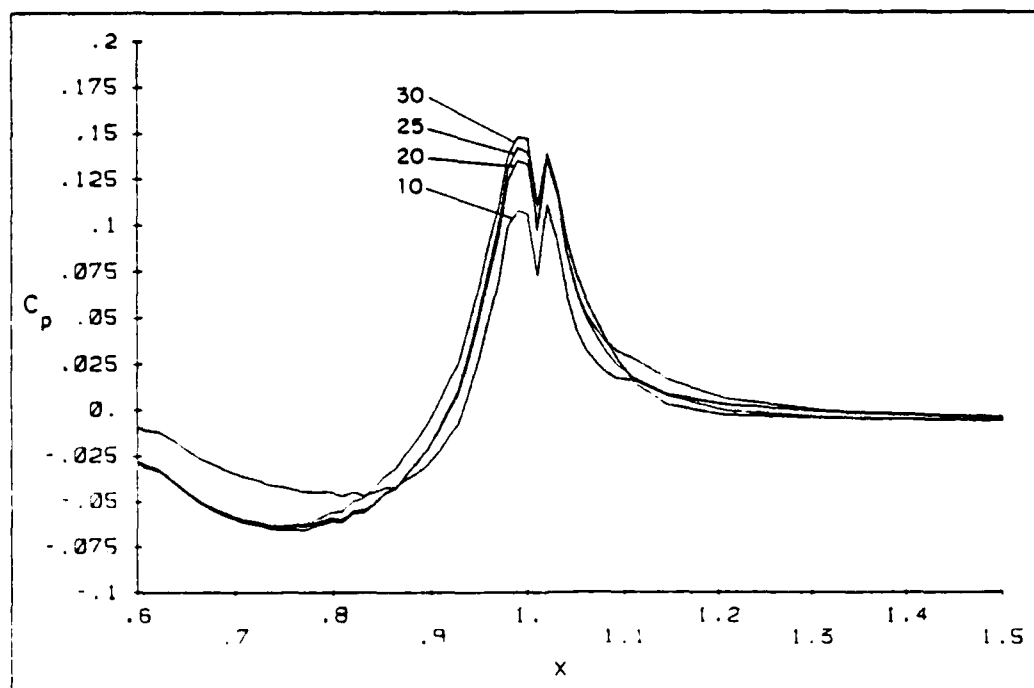


Figure 15. Convergence History of the Pressure Distribution on the Surface of the Body and Along the Wake Centerline: Minor Axis Plane, Interaction Solution.

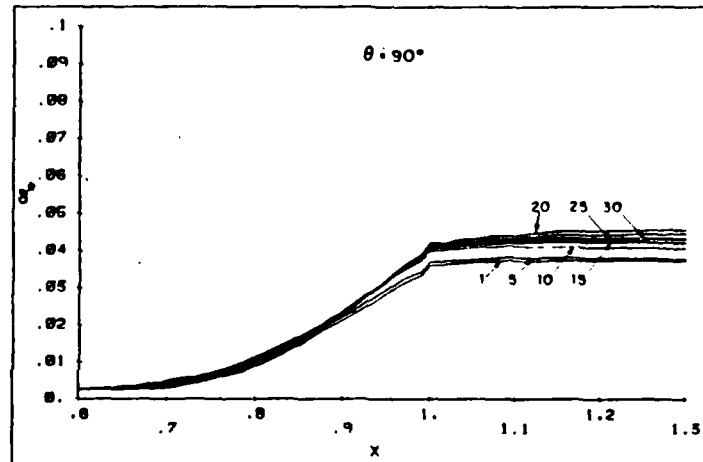


Figure 16. Convergence History of the Displacement Thickness: Major Axis Plane, Interaction Solution.

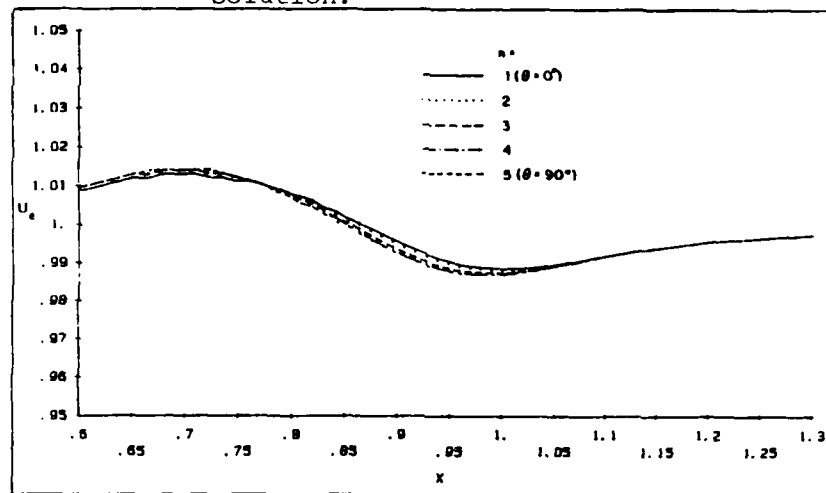


Figure 17. Edge Velocity.

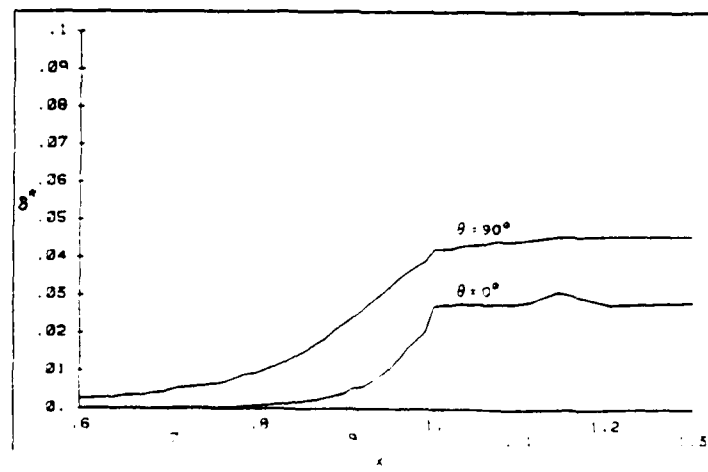


Figure 18. Displacement Thickness: Minor and Major Axes Planes, Interaction Solution.



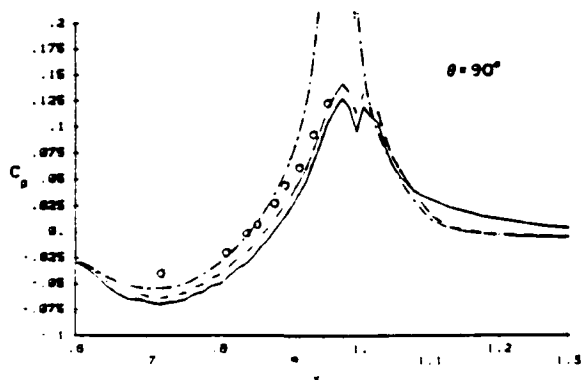
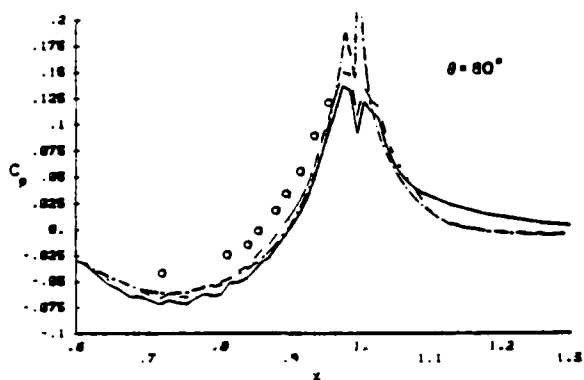
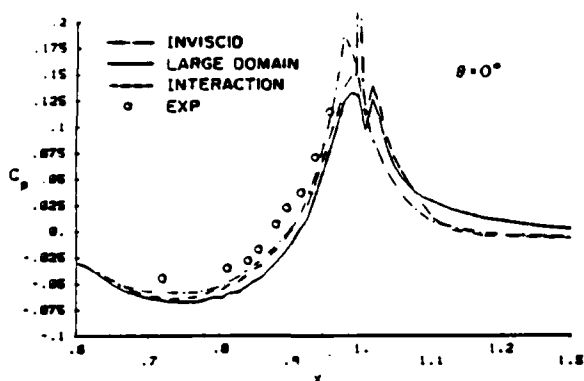


Figure 19. Pressure Distribution on the Surface of the Body and Along the Wake Centerline.

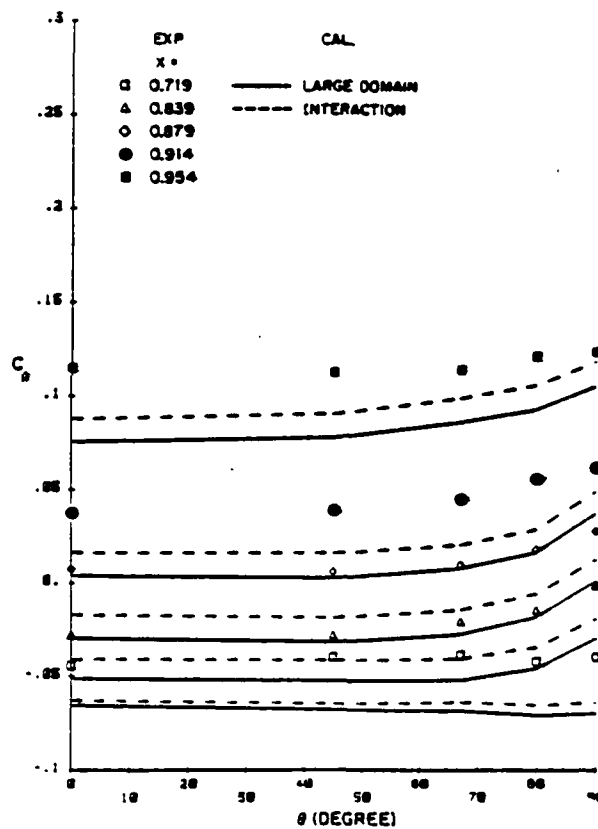


Figure 20. Girthwise Variation of Pressure on the 3:1 Body.

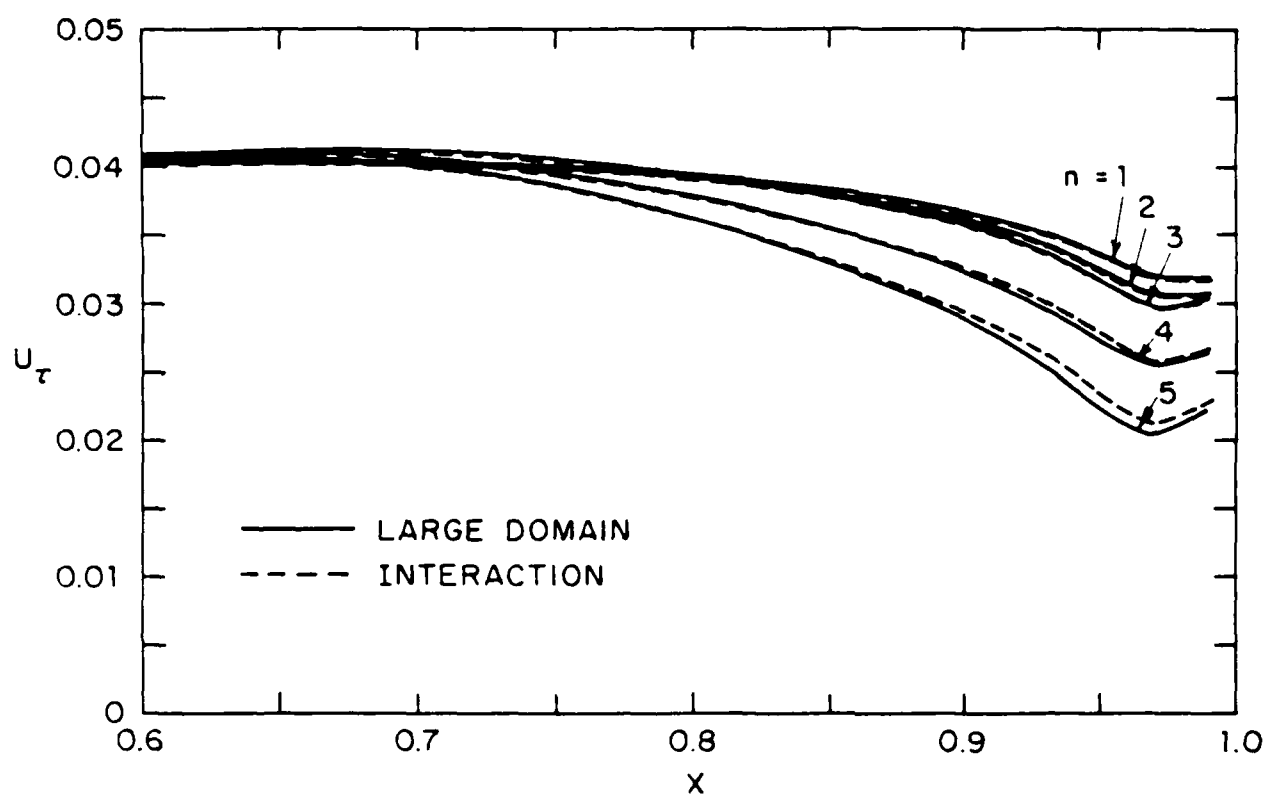


Figure 21. Wall-Shear Velocity.

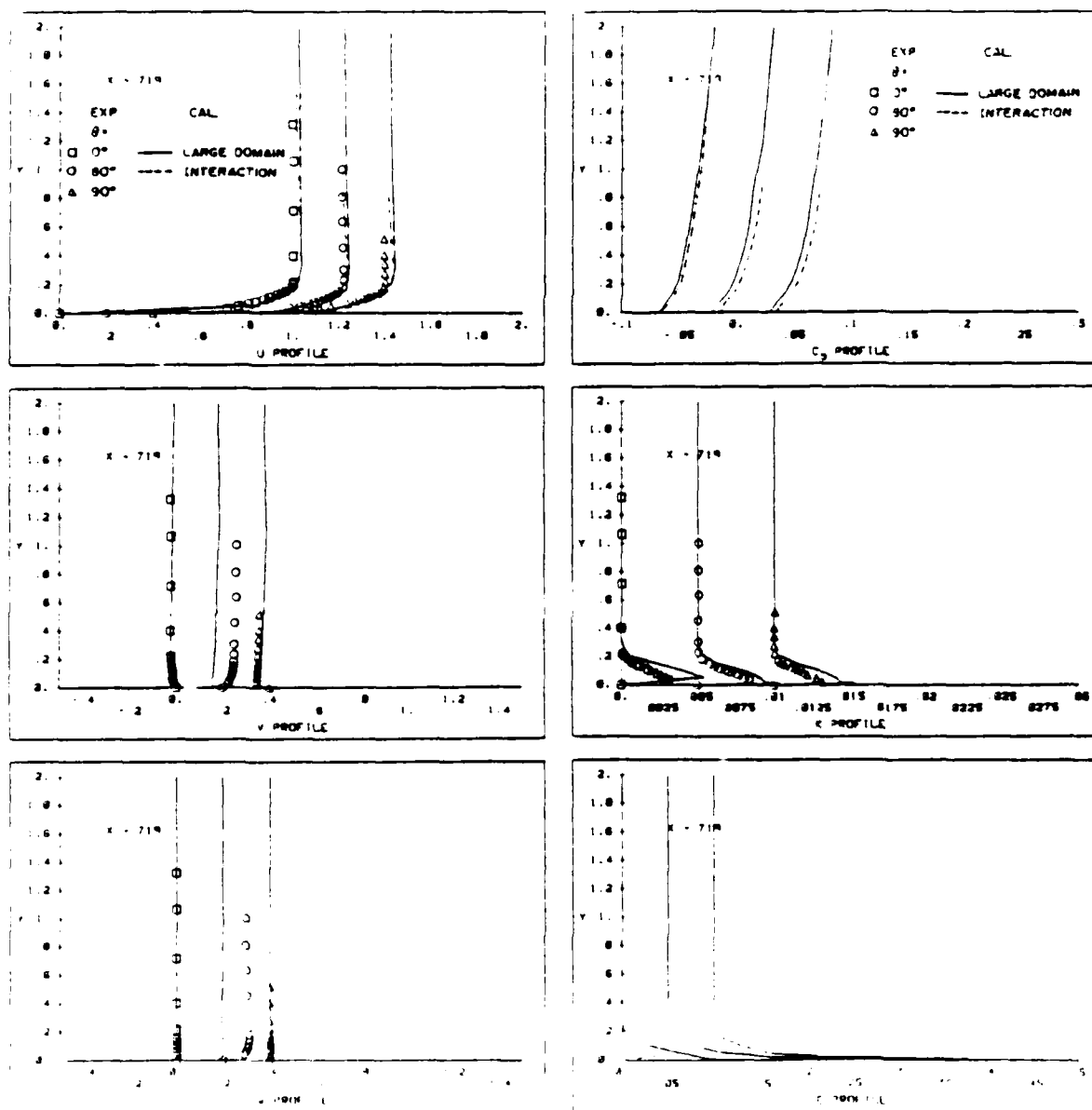


Figure 22. Solution Profiles.

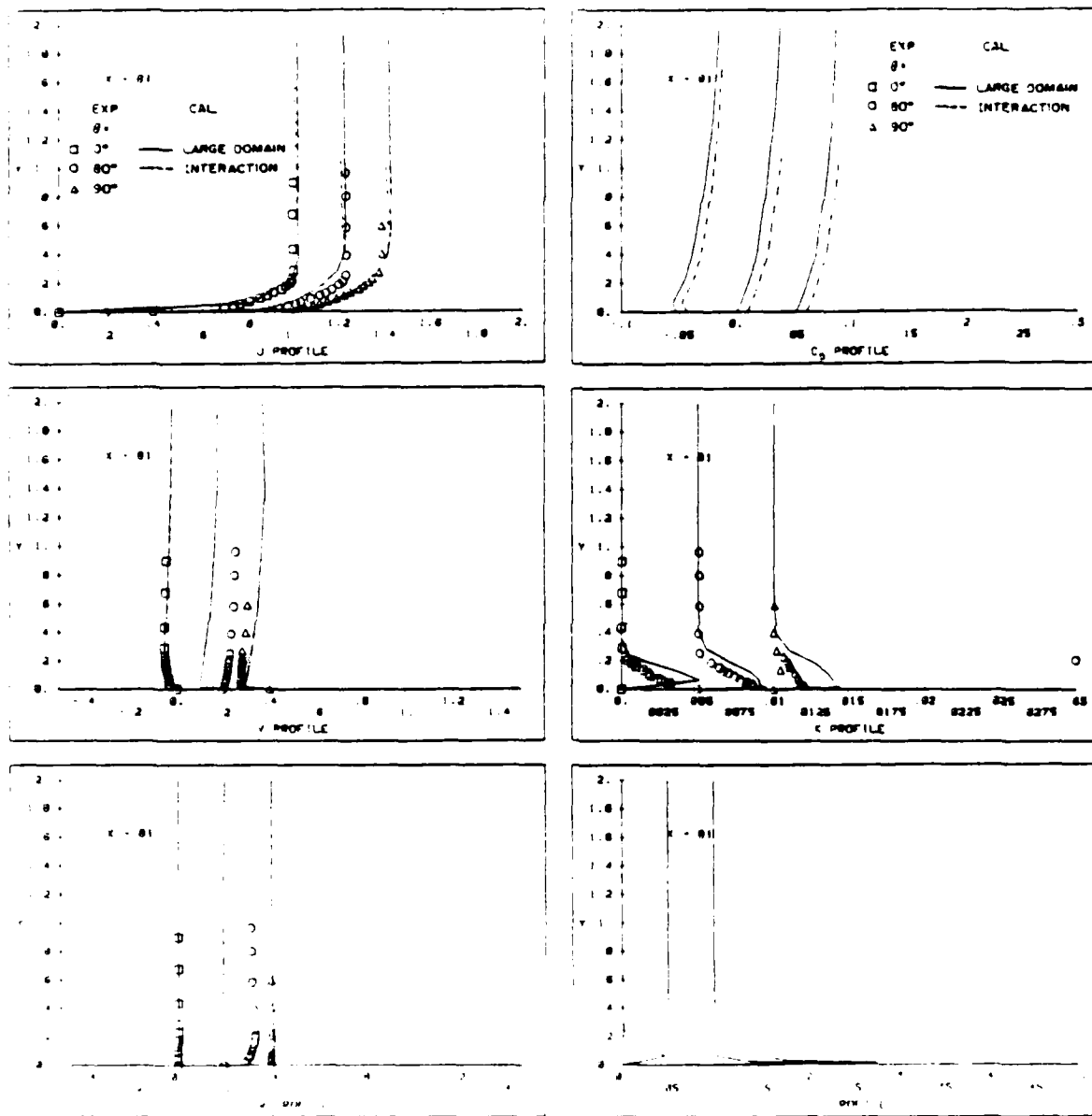


Figure 22. (Continued).

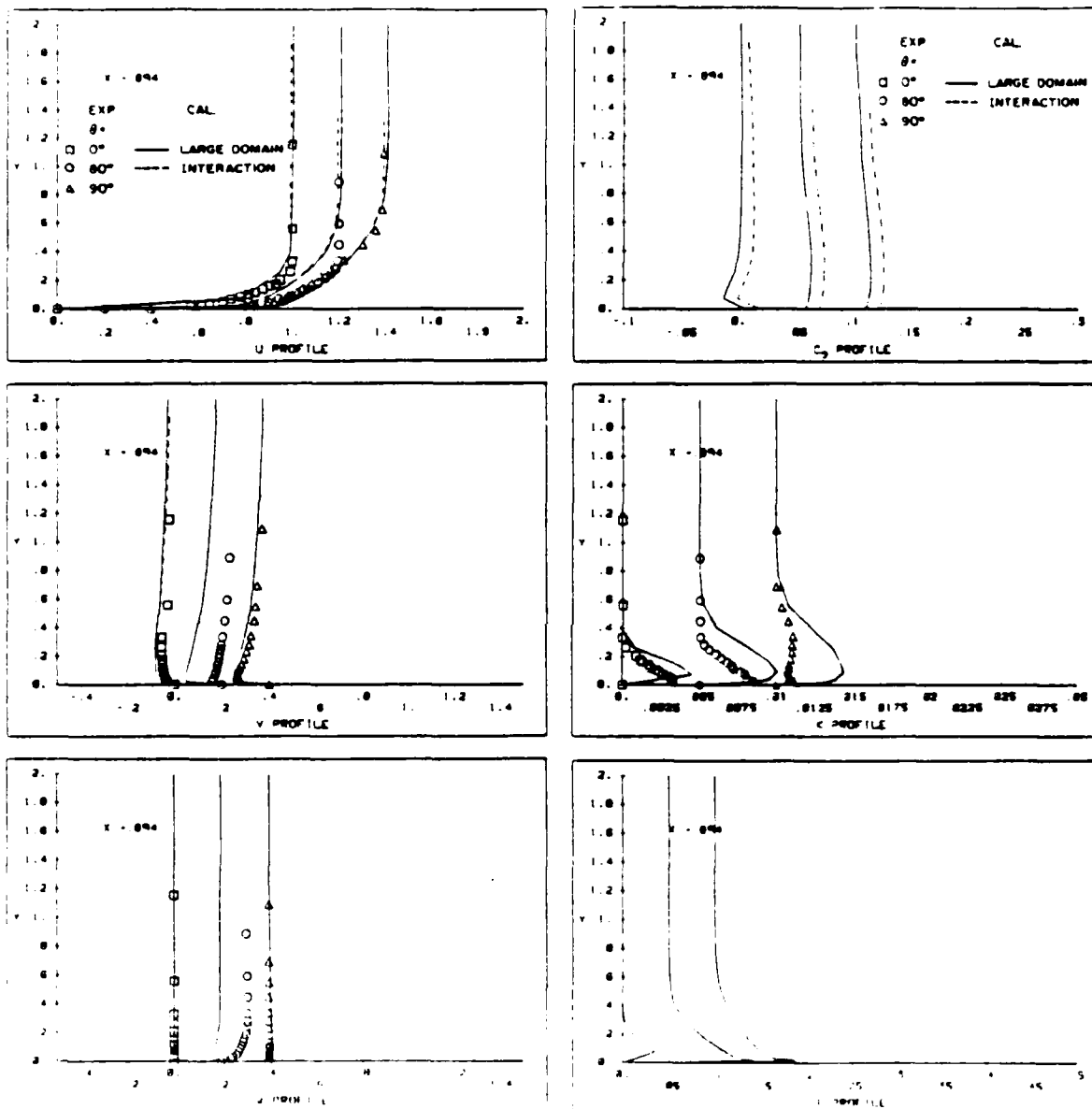


Figure 22. (Continued).

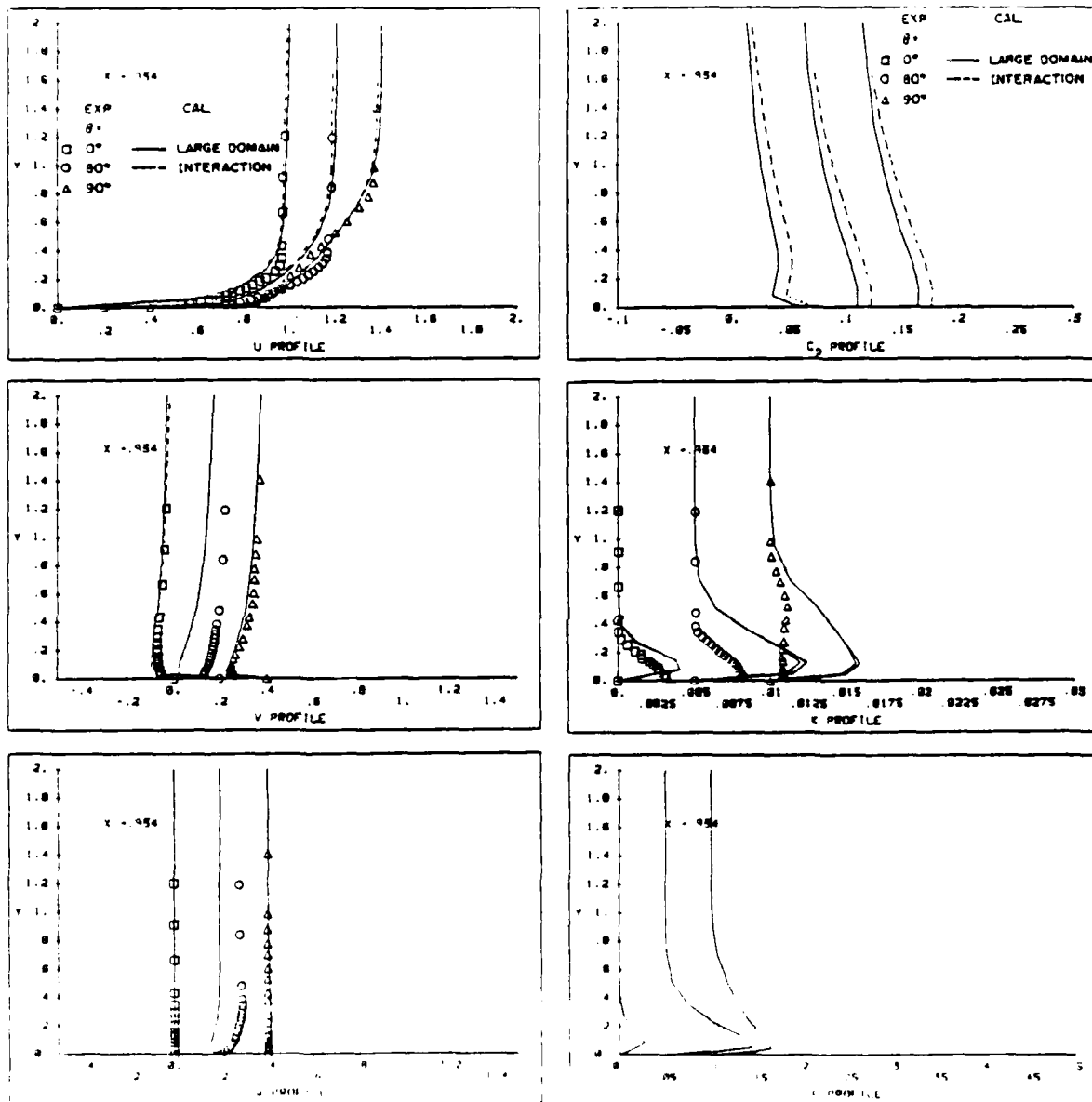


Figure 22. (Continued).

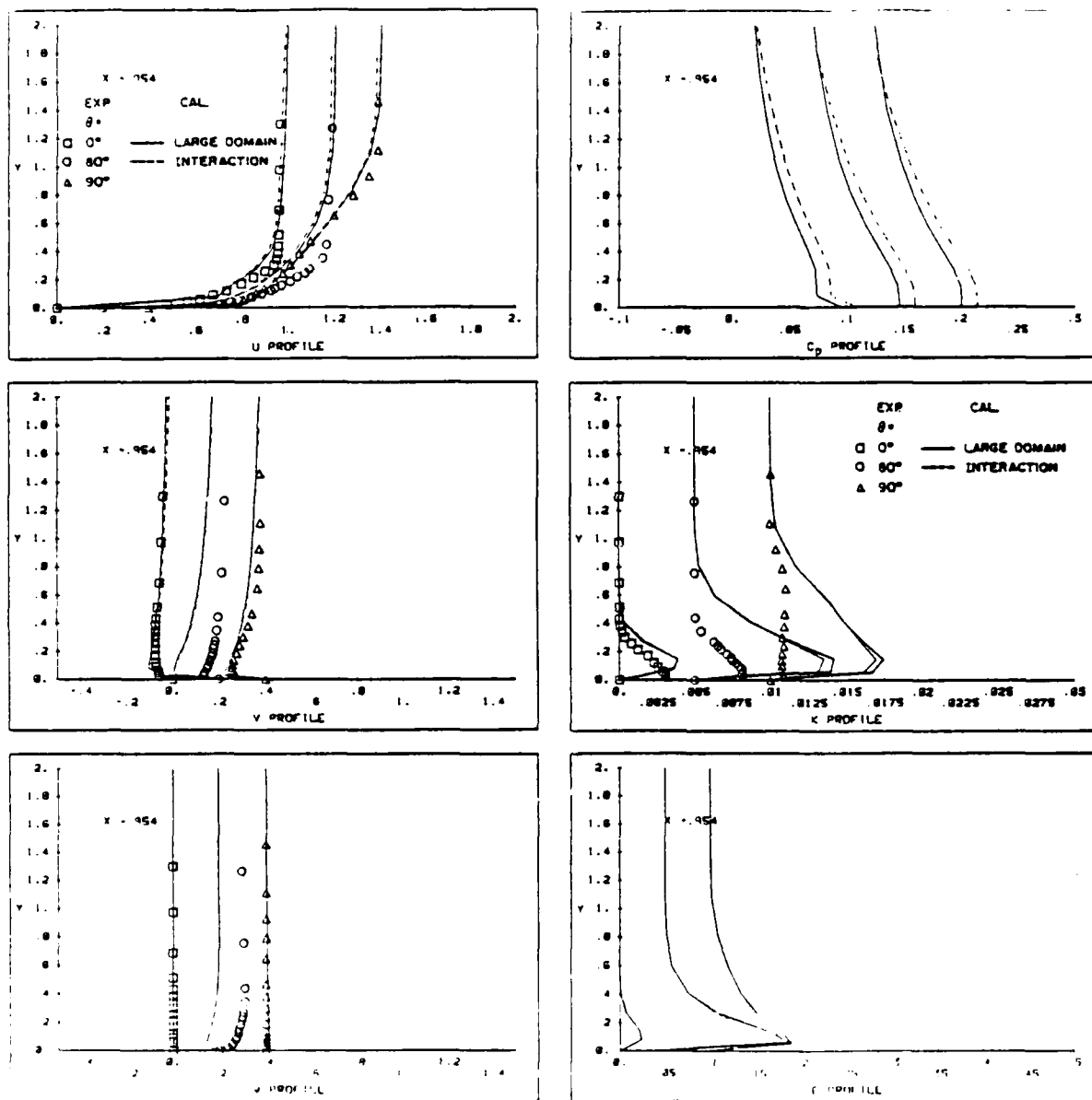


Figure 22. (Continued).

# APPENDIX I: Corrections to Stern et al. (1986)

This appendix provides corrections to errors in the text of Stern et al. (1986) which were discovered after printing.

- 1) p. 10 line 1, equation (III-3) should read:

$$\delta^* = \int_0^{\delta} (1 - U/U_e) dy$$

- 2) p. 32 line 5, equation (V-6) should read:

$$G = -1/R$$

$$R = |\underline{X} - \underline{\xi}|$$

- 3) p. 32 line 10, equation (V-7) should read:

$$2\pi\sigma - \int_{S_B} \sigma \frac{\partial G}{\partial n} dS = -U_o n_1$$

- 4) p. 35 line 16, in equation (V-12)  $\sigma$  is defined by:

$$\sigma = \frac{1}{2\pi} \frac{d}{dx} (U_e \delta^*)$$

- 5) p. 112 line 19, the equation should read:

$$(U_1, V_1, W_1) = \left( \frac{\partial U}{\partial x_1}, \frac{\partial V}{\partial x_1}, \frac{\partial W}{\partial x_1} \right)$$

- 6) p. 115 line 7, in equation (B-1) the term  $R_4^2 U^2$  should read:

$$R_4 U^2$$

- 7) P. 117 lines 18 and 19, equation (B-9) should read:

$$\epsilon_{12} = \frac{1}{2} \left[ \frac{h_1}{s} \{A U b_{11} + H(U b_{12} + V_2) + G(U b_{13} + V_3)\} \right]$$



$$+ \frac{h_2}{s} \{H(U_1 + U_{a11}) + B(U_2 + U_{a12}) + F(U_3 + U_{a13})\} \quad (B-9)$$

8) p. 117 lines 20 and 21, equation (B-10) should read:

$$\begin{aligned} \epsilon_{13} = & \frac{1}{2} \left[ \frac{h_1}{s} \{A U_{c11} + H(U_{c12} + W_2) + G(U_{c13} + W_3)\} \right. \\ & \left. + \frac{h_3}{s} \{G(U_1 + U_{a11}) + F(U_2 + U_{a12}) + C(U_3 + U_{a13})\} \right] \quad (B-10) \end{aligned}$$

9) p. 118 lines 2 and 3, equation (B-12) should read:

$$\begin{aligned} \epsilon_{23} = & \frac{1}{2} \left[ \frac{h_2}{s} \{H U_{c11} + B(U_{c12} + W_2) + F(U_{c13} + W_3)\} + \frac{h_3}{s} \{G U_{b11} + F(U_{b12} + V_2) \right. \\ & \left. + C(U_{b13} + V_3)\} \right] \quad (B-12) \end{aligned}$$

10) p. 125 line 16, in the equation the term  $-\frac{2}{3} \frac{\partial k_{22}}{h_2 \partial y}$  should read:

$$-\frac{2}{3} \frac{\partial \bar{k}_{22}}{h_2 \partial y}$$

11) p. 128 line 7, in the equation the term  $S_2(\frac{2}{3} k_{33} - 2v_t \epsilon_{33})$  should read:

$$S_2(\frac{2}{3} \bar{k}_{33} - 2v_t \epsilon_{33})$$

12) p. 131 line 5, in the equation the term  $\frac{1}{h_3} \frac{\partial}{\partial z} (v_t \epsilon_{33})$  should read:

$$\frac{1}{h_3} \frac{\partial}{\partial z} (v_t \bar{\epsilon}_{33})$$

## APPENDIX II. Modifications of Equations in Discretized Form for Three-Dimensional Flow

As discussed in Section III, some modifications of the finite-difference formulas presented in Appendix III of Stern et al. (1986) were found to be necessary upon performing calculations for three-dimensional bodies. These are provided below:

- 1) p. 126 lines 1 and 2, in the right hand side of equation (C-15)  $\epsilon_{23}$  should be replaced by  $\bar{\epsilon}_{23}$ , where

$$\bar{\epsilon}_{23} = \epsilon_{23} - \frac{1}{2h_3} \frac{\partial v}{\partial z}$$

- 2) p. 126 after line 5, the following equation should be inserted:

$$\begin{aligned} \frac{\partial}{h_3 \partial z} \left( v_t \frac{\partial v}{h_3 \partial z} \right) &= \frac{\partial}{h_3 \partial z} \left( \frac{v_t}{h_3} \right) \frac{\partial v}{\partial z} + \frac{v_t}{h_3^2} \frac{\partial^2 v}{\partial z^2} \\ &= \frac{1}{2} \left\{ \frac{\partial}{h_3 \partial z} \left( \frac{v_t}{h_3} \right) \right\}_m^{\ell} - \frac{1}{2} (v_{m,n+1}^{\ell} - v_{m,n-1}^{\ell}) \\ &\quad + \left( \frac{v_t}{h_3} \right)_m^{\ell} - \frac{1}{2} (v_{m,n+1}^{\ell} - 2v_{m,n}^{\ell} + v_{m,n-1}^{\ell}) = yd_5 - yd_6 v_{m,n}^{\ell} \end{aligned} \quad (C-16-1)$$

- 3) p. 128 line 7, the right hand side of equation (C-21) should read:

$$= yf_6 - yf_7 v_{m,n}^{\ell} \quad (CD), \quad (CD) \quad (C-21)$$

- 4) p. 128 line 12, the right hand side of equation (C-22) should read:

$$= yg_1 + yg_2 v_{m,n}^{\ell} \quad (C-22)$$

- 5) p. 129 lines 2-13, should be replaced by:

Collecting all terms (C-12) - (C-23):

$$\begin{aligned}
 & ya_1(V_{m,n}^{\ell} - V_{m,n}^{\ell-1}) + yb_1 V_{m+1,n}^{\ell} - yb_2 V_{m,n}^{\ell} + yb_3 V_{m-1,n}^{\ell} + yc_1 + yd_1 \\
 & - yd_2 V_{m+1,n}^{\ell} + yd_3 V_{m,n}^{\ell} - yd_4 V_{m-1,n}^{\ell} - yd_5 + yd_6 V_{m,n}^{\ell} + ye_1 - yf_1 V_{m+1,n}^{\ell} + yf_2 V_{m,n}^{\ell} \\
 & - yf_3 V_{m-1,n}^{\ell} - yf_4 - yf_5 - yf_6 + yf_7 V_{m,n}^{\ell} + yg_1 - yh_1 + yg_2 V_{m,n}^{\ell} = 0
 \end{aligned}$$

or

$$\begin{aligned}
 & (yb_3 - yd_4 - yf_3) V_{m-1,n}^{\ell} + (ya_2 - yb_2 + yd_3 + yd_6 + yf_2 + yf_7 + yg_2) V_{m,n}^{\ell} \\
 & + (yb_1 - yd_2 - yf_1) V_{m+1,n}^{\ell} = ya_1 V_{m,n}^{\ell-1} - yc_1 - yd_1 + yd_5 - ye_1 + yf_4 + yf_5 + yf_6 - yg_1 + yh_1
 \end{aligned}$$

Finally, the coefficients in equation (IV-19) are:

$$b_1 = yb_3 - yd_4 - yf_3$$

$$b_2 = ya_1 - yb_2 + yd_3 + yd_6 + yf_2 + yf_7 + yg_2 \quad (C-24)$$

$$b_3 = yb_1 - yd_2 - yf_1$$

$$Sv = ya_1 V_{m,n}^{\ell-1} - yc_1 - yd_1 + yd_5 + yd_6 + yf_4 + yf_5 + yf_6 - yg_1 + yh_1$$

$$Pv = - ye_1$$

6) p. 131 lines 6 and 7, in the right hand side of equation (C-28)  $\epsilon_{23}$  should be replaced by  $\bar{\epsilon}_{23}$ , where

$$\bar{\epsilon}_{23} = \epsilon_{23} - \frac{1}{2h_2} \frac{\partial W}{\partial y}$$

7) p. 132 after line 1, the following equation should be inserted:

$$\frac{\partial}{h_2 \partial y} \left( \frac{v_t}{h_2} \frac{\partial W}{\partial y} \right) = \frac{\partial}{h_2 \partial y} \left( \frac{v_t}{h_2} \right) \frac{\partial W}{\partial y} + \frac{v_t}{h_2^3} \frac{\partial^2 W}{\partial y^2}$$

$$= \frac{1}{2} \left\{ \frac{\partial}{\partial y} \left( \frac{v_t}{h_2} \right) \right\}_{m,n}^{\ell - \frac{1}{2}} (W_{m+1,n}^{\ell} - W_{m-1,n}^{\ell}) + \left( \frac{v_t}{h_2} \right)_{m,n}^{\ell - \frac{1}{2}}$$

$$(W_{m+1,n}^{\ell} - 2W_{m,n}^{\ell} + W_{m-1,n}^{\ell}) = zd_5 - zd_6 W_{m,n}^{\ell} \quad (CD) \quad (C-29-1)$$

8) p. 132 line 14, the right hand side of equation (C-31) should read:

$$= zf_1 - zf_7 W_{m,n}^{\ell} \quad (CD) \quad (C-31)$$

9) p. 133 line 18, the right hand side of equation (C-35) should read:

$$= zg_1 + zg_2 W_{m,n}^{\ell} \quad (C-35)$$

10) p. 134 lines 5-18, should be replaced by

Collecting all the terms (C-25) - (C-36):

$$\begin{aligned} & za_1 (W_{m,n}^{\ell} - W_{m,n}^{\ell-1}) + zb_1 + zc_1 W_{m,n+1}^{\ell} - zc_2 W_{m,n}^{\ell} + zc_3 W_{m,n-1}^{\ell} \\ & + zd_1 - zd_2 W_{m,n+1}^{\ell} + zd_3 W_{m,n}^{\ell} - zd_4 W_{m,n-1}^{\ell} - zd_5 + zd_6 W_{m,n}^{\ell} + ze_1 - zf_1 - zf_2 - zf_3 \\ & - zf_4 W_{m,n+1}^{\ell} + zf_5 W_{m,n}^{\ell} - zf_6 W_{m,n-1}^{\ell} + zf_7 W_{m,n}^{\ell} + zg_1 + zg_2 W_{m,n}^{\ell} - zh_1 = 0 \end{aligned}$$

or

$$\begin{aligned} & (zc_3 - zd_4 - zf_6) W_{m,n-1}^{\ell} + (za_1 - zc_2 + zd_3 + zd_6 + zf_5 + zf_7 + zg_2) W_{m,n}^{\ell} \\ & + (zc_1 - zd_2 - zf_4) W_{m,n+1}^{\ell} = za_1 W_{m,n}^{\ell-1} - zb_1 - zd_1 + zd_5 + zf_1 + zf_2 + zf_3 \\ & - zg_1 - ze_1 - zh_1 \end{aligned}$$

Finally, the coefficients in equation (IV-20) are:

$$c_1 = zc_3 - zd_4 - zf_6$$

$$c_2 = za_1 - zc_2 - zd_3 + zd_6 + zf_5 + zf_7 + zg_2$$

$$c_3 = zc_1 - zd_2 - zf_4 \quad (C-37)$$

$$Pw = -ze_1$$

$$Sw = za_1 W_{m,n}^{\ell-1} - zb_1 - zd_1 + zd_5 + zf_1 + zf_2 + zf_3 - zg_1 + zh_1$$

11) p. 137 line 4, the right hand side of equation (C-44) should read:

$$= Fd_6 - Fd_7 F_{m,n}^{\ell} \quad (CD) \quad (C-44)$$

12) p. 137 lines 13-15, should be replaced by:

$$+ Fd_2 F_{m,n}^{\ell} - Fd_3 F_{m-1,n}^{\ell} - Fd_4 - Fd_5 - Fd_6 + Fd_7 F_{m,n}^{\ell} - Fe_1 + Fe_2 F_{m,n}^{\ell} = 0$$

or

$$-(Fb_1 + Fd_3) F_{m-1,n}^{\ell} + (Fa_1 + Fd_2 + Fd_7 + Fe_2) F_{m,n}^{\ell} + (Fb_1 - Fd_1) F_{m+1,n}^{\ell}$$

13) p. 138 line 3, should be replaced by:

$$(d,e)_2 = Fa_1 + Fd_2 + Fd_7 + Fe_2 \quad (C-47)$$

DISTRIBUTION LIST FOR TECHNICAL REPORTS  
ONR FLUID DYNAMIC PROGRAM (HYDRODYNAMICS)

Defense Technical Information Center  
Information Facility  
Alexandria, VA 22314  
12 copies

NASA Scientific and Technical  
Information Facility  
P.O. Box 8757  
Baltimore/Washington International Airport  
Maryland 21240

Office of Naval Research  
Code 432F  
800 N. Quincy Street  
Arlington, VA 22217  
3 copies

Librarian  
University of California  
Department of Naval Architecture  
and Offshore Engineering  
Berkeley, CA 94720

Professor Bruce Johnson  
U.S. Naval Academy  
Hydromechanics Laboratory  
Annapolis, MD 21402

Library  
David Taylor Naval Ship Research  
and Development Center  
Code 522.1  
Bethesda, MD 20084

Library  
U.S. Naval Academy  
Annapolis, MD 21402

The Society of Naval Architects and  
Marine Engineers  
One World Trade Center, Suite 1369  
New York, NY 10048

Technical Library  
Webb Institute of Naval Architecture  
Glen Cove, NY 11542

Technical Library  
Naval Coastal System Center  
Panama City, FL 32401

Library  
Stevens Institute of Technology  
Davidson Laboratory  
Castle Point Station  
Hoboken, NJ 07030

Technical Library  
Naval Ship Engineering Center  
Philadelphia Division  
Philadelphia, PA 19112

R.E. Gibson Library  
The Johns Hopkins University  
Applied Physics Laboratory  
Johns Hopkins Road  
Laurel, MD 20810

Editor  
Applied Mechanics Review  
Southwest Research Institute  
8500 Culebra Road  
San Antonio, TX 78206

Lorenz G. Straub Library  
University of Minnesota  
St. Anthony Falls Hydraulic Laboratory  
Minneapolis, MN 55414

Technical Library  
Naval Ocean Systems Center  
San Diego, CA 92152

Library  
Naval Postgraduate School  
Monterey, CA 93940

Librarian  
Naval Surface Weapons Center  
White Oak Laboratory  
Silver Spring, MD 20910

Technical Library  
Naval Underwater Systems Center  
Newport, RI 02840

Library  
Department of Ocean Engineering  
Massachusetts Institute of Technology  
Cambridge, MA 01778

Engineering Societies Library  
345 East 47th Street  
New York, NY 10017

Library  
Department of Naval Architecture  
and Marine Engineering  
University of Michigan  
Ann Arbor, MI 48109

Librarian Station 5-2  
Coast Guard Headquarters  
NASSIF Building  
400 Seventh Street, SW  
Washington, DC 20591

Library  
Applied Research Laboratory  
The Pennsylvania State University  
P.O. Box 30  
State College, PA 16801

Library of Congress  
Science and Technology Division  
Washington, DC 20540

Library  
Marine Physical Laboratory  
Scripps Institution of Oceanography  
University of California @ San Diego  
San Diego, CA 92152

Dr. A.L. Slafkosky  
Scientific Advisor  
Commandant of the Marine Corps  
Code AX  
Washington, DC 20380

Library  
Applied Research Laboratories  
University of Texas at Austin  
Austin, TX 78712

Maritime Administration  
Office of Maritime Technology  
14th & E Streets, NW  
Washington, DC 20230

Library  
Woods Hole Oceanographic Institution  
Woods Hole, MA 02543

Maritime Administration  
Division of Naval Architecture  
14th & E Streets, NW  
Washington, DC 20230

Professor Robert E. Falco  
Michigan State University  
Department of Mechanical Engineering  
East Lansing, MI 48824

Naval Research Laboratory  
Code 2627  
Washington, DC 20375

Mr. Dennis Bushnell  
NASA Langley Research Center  
Langley Station  
Hampton, VA 23365

Library  
Naval Sea Systems Command  
Code 09GS  
Washington, DC 20362

Dr. A.K.M. Fazle Hussain  
University of Houston  
Department of Mechanical Engineering  
Houston, TX 77004

Library  
Institute of Hydraulic Research  
The University of Iowa  
Iowa City, IA 52242

Professor John L. Lumley  
Cornell University  
Sibley School of Mechanical and Aerospace  
Engineering  
Ithaca, NY 14853

Library  
Southwest Research Institute  
8500 Culebra Road  
San Antonio, TX 78228

Professor W.W. Willmarth  
The University of Michigan  
Department of Aerospace Engineering  
Ann Arbor, MI 48109

Professor A. Roshko  
California Institute of Technology  
Graduate Aeronautical Laboratories  
Pasadena, CA 91125

Professor Stanley Corrsin  
The Johns Hopkins University  
Department of Chemical Engineering  
Baltimore, MD 21218

Professor J.T.C. Liu  
Brown University  
Division of Engineering  
Providence, RI 02912

Professor Patrick Leehey  
Massachusetts Institute of Technology  
Department of Ocean Engineering  
Cambridge, MA 02139

Dr. W.C. Lin  
Code 152  
DTNSRDC  
Bethesda, MD 20084

Professor Eli Reshotko  
Case Western Reserve University  
Department of Mechanical and  
Aerospace Engineering  
Cleveland, OH 44106

Mr. J.H. McCarthy  
Code 154  
DTNSRDC  
Bethesda, MD 20084

Dr. Steven A. Orszag  
Cambridge Hydrodynamics, Inc.  
P.O. Box 1403  
Princeton, NJ 08542

Mr. D.S. Cieslowski  
Code 156  
DTNSRDC  
Bethesda, MD 20084

Professor Tuncer Cebeci  
California State University  
Mechanical Engineering Department  
Long Beach, CA 90840

Mr. V.J. Monacella  
Code 1504  
DTNSRDC  
Bethesda, MD 20084

Dr. C.W. Hirt  
University of California  
Los Alamos Scientific Laboratory  
P.O. Box 1663  
Los Alamos, NM 87544

Dr. B. Yim  
Code 154.1  
DTNSRDC  
Bethesda, MD 20084

Dr. Hans Lugt  
Code 1802  
DTNSRDC  
Bethesda, MD 20084

Dr. H. Haussling  
Code 1843  
DTNSRDC  
Bethesda, MD 22084

Mr. W.C. Sandberg  
Code 55W33  
Naval Sea Systems Command  
Washington, DC 20362

Prof. Marshall P. Tulin  
Department of Mechanical and  
Environmental Engineering  
University of California at Santa Barbara  
Santa Barbara, CA 93106

Mr. E.N. Comstock  
Code 55W3  
Naval Sea Systems Command  
Washington, DC 20362

Prof. Jin Wu  
College of Marine Studies  
University of Delaware  
Lewes, DE 19958



Dr. R.J. Hansen  
Code 5844  
Naval Research Laboratory  
Washington, DC 20375

Prof. S.G. Rubin  
Department of Aerospace Engineering  
and Applied Mechanics  
University of Cincinnati  
Cincinnati, OH 45221

Dr. O.M. Griffin  
Code 5841  
Naval Research Laboratory  
Washington, DC 20375

Professor S.F. Shen  
Sibley School of Mechanical and  
Aerospace Engineering  
Cornell University  
Ithaca, NY 14850

Dr. T.F. Zien  
Code R44  
Naval Surface Weapons Center  
White Oak Lab.  
Silver Spring, MD 20910

Prof. J.E. Kerwin  
Department of Ocean Engineering  
Massachusetts Institute of Technology  
Cambridge, MA 01778

Dr. W.K. Blake  
Code 1905.1  
DTNSRDC  
Bethesda, MD 20854

Prof. C.M. Ho  
Department of Aerospace Engineering  
University of Southern California  
University Park  
Los Angeles, CA 90007  
2 copies

Dr. Do C. Kwak  
Applied Computational Aerodynamics  
Branch  
NASA Ames Research Center  
M/S 202A-14  
Moffet Field, CA 94035

Prof. V.C. Patel  
Institute of Hydraulic Research  
The University of Iowa  
Iowa City, IA 52242  
2 copies

Prof. P.G. Saffman  
Department of Applied Mathematics  
California Institute of Technology  
Pasadena, CA 91125

Dr. N. Salvesen  
Science Applications, Inc.  
134 Holiday Court, Suite 318  
Annapolis, MD 21401

Prof. O.M. Phillips  
Dept. of Earth & Planetary Science  
Johns Hopkins University  
Baltimore, MD 21218

Prof. P.M. Naghdi  
Dept. of Mechanical Engineering  
University of California  
Berkeley, CA 94720

Dr. T.D. Taylor  
Applied Physics Laboratory  
Johns Hopkins University  
Baltimore, MD 21218

Dr. T.T. Huang  
Code 1542  
DTNSRDC  
Bethesda, MD 20084

Prof. W.G. Tiederman  
School of Mechanical Engineering  
Purdue University  
West Lafayette, IN 47907

Prof. R.W. Yeung  
Dept. of Naval Architecture  
and Offshore Engineering  
University of California  
Berkeley, CA 94720  
3 copies

Prof. R.L. Street  
Dept. of Civil Engineering  
Stanford University  
Stanford, CA 94305

Prof. W.R. Schowalter  
Dept. of Chemical Engineering  
Princeton University  
Princeton, NJ 08540

Prof. T. Maxworthy  
Dept. of Mechanical Engineering  
University of Southern California  
University Park  
Los Angeles, CA 90089-0192

Prof. J. Schetz  
Dept. of Aerospace & Ocean Engineering  
Virginia Polytechnic Institute and  
State University  
Blacksburg, VA 24061  
2 copies

Prof. D. Rockwell  
Dept. of Mechanical Engineering  
and Mechanics  
Lehigh University  
Bethlehem, PA 18015

Dr. E.P. Rood  
Code 1543  
DTNSRDC  
Bethesda, MD 20084

Prof. J.B. Keller  
Dept. of Mathematics  
Stanford University  
Stanford, CA 94305

Prof. A.J. Acosta  
Dept. of Mechanical Engineering  
California Institute of Technology  
Pasadena, CA 91125

Prof. J.N. Newman  
Dept. of Ocean Engineering  
Massachusetts Institute of Technology  
Cambridge, MA 01778

Prof. J.L. Kerwin  
Dept. of Ocean Engineering  
Massachusetts Institute of Technology  
Cambridge, MA 01778

Dr. S.J. Shamroth  
Scientific Research Associates, Inc.  
P.O. Box 498  
Glastonburg, CT 06033

Prof. W.S. Vorus  
Dept. of Naval Architecture and  
Marine Engineering  
University of Michigan  
Ann Arbor, MI 48109

Prof. A.H. Nayfeh  
Dept. of Engineering Sciences & Mechanics  
Virginia Polytechnic Institute and  
State University  
Blacksburg, VA 24061

Prof. T.Y. Wu  
Dept. of Engineering Science  
California Institute of Technology  
Pasadena, CA 91125

Prof. C.C. Mei  
Dept. of Civil Engineering  
Massachusetts Institute of Technology  
Cambridge, MA 02139

Prof. S.A. Berger  
Dept. of Mechanical Engineering  
University of California  
Berkeley, CA 94720

Prof. J.W. Miles  
Dept. of Geophysics  
University of California  
La Jolla, CA 92093

Dr. J.H. Duncan  
Flow Research Company  
1320 Fenwick Lane, Suite 401  
Silver Spring, MD 20910

Prof. C.E. Brennen  
Dept. of Mechanical Engineering  
California Institute of Technology  
Pasadena, CA 91125

Prof. R.F. Beck  
Dept. of Naval Architecture and  
Marine Engineering  
University of Michigan  
Ann Arbor, MI 48109

Prof. T. Sarpkaya  
Dept. of Mechanical Engineering  
Code 69-SL  
Naval Postgraduate School  
Monterey, CA 93940

Dr. D. Savitsky  
Davidson Laboratory  
Steve: Institute of Technology  
Hoboken, NJ 07030  
2 copies

END

4-87

DTIC